



Calhoun: The NPS Institutional Archive DSpace Repository

Theses and Dissertations

1. Thesis and Dissertation Collection, all items

2008-12

Real time imaging analysis using a terahertz quantum cascade laser and a microbolometer focal plane array

Buchanan, Kevin William.

Monterey California. Naval Postgraduate School

<http://hdl.handle.net/10945/3813>

Downloaded from NPS Archive: Calhoun



<http://www.nps.edu/library>

Calhoun is the Naval Postgraduate School's public access digital repository for research materials and institutional publications created by the NPS community.

Calhoun is named for Professor of Mathematics Guy K. Calhoun, NPS's first appointed -- and published -- scholarly author.

Dudley Knox Library / Naval Postgraduate School
411 Dyer Road / 1 University Circle
Monterey, California USA 93943



**NAVAL
POSTGRADUATE
SCHOOL**

MONTEREY, CALIFORNIA

THESIS

**REAL TIME IMAGING ANALYSIS USING A TERAHERTZ
QUANTUM CASCADE LASER AND A
MICROBOLOMETER FOCAL PLANE ARRAY**

by

Kevin William Buchanan

December 2008

Thesis Advisor:
Co-Advisor:

Gamani Karunasiri
Scott Davis

Approved for public release; distribution is unlimited

THIS PAGE INTENTIONALLY LEFT BLANK

REPORT DOCUMENTATION PAGE
Form Approved OMB No. 0704-0188

Public reporting burden for this collection of information is estimated to average 1 hour per response, including the time for reviewing instruction, searching existing data sources, gathering and maintaining the data needed, and completing and reviewing the collection of information. Send comments regarding this burden estimate or any other aspect of this collection of information, including suggestions for reducing this burden, to Washington Headquarters Services, Directorate for Information Operations and Reports, 1215 Jefferson Davis Highway, Suite 1204, Arlington, VA 22202-4302, and to the Office of Management and Budget, Paperwork Reduction Project (0704-0188) Washington DC 20503.

1. AGENCY USE ONLY (Leave blank)	2. REPORT DATE December 2008	3. REPORT TYPE AND DATES COVERED Master's Thesis
4. TITLE AND SUBTITLE Real Time Imaging Analysis using a THz Quantum Cascade Laser and a Microbolometer Focal Plane Array		5. FUNDING NUMBERS
6. AUTHOR(S) Kevin William Buchanan		
7. PERFORMING ORGANIZATION NAME(S) AND ADDRESS(ES) Naval Postgraduate School Monterey, CA 93943-5000		8. PERFORMING ORGANIZATION REPORT NUMBER
9. SPONSORING /MONITORING AGENCY NAME(S) AND ADDRESS(ES) N/A		10. SPONSORING/MONITORING AGENCY REPORT NUMBER
11. SUPPLEMENTARY NOTES The views expressed in this thesis are those of the author and do not reflect the official policy or position of the Department of Defense or the U.S. Government.		
12a. DISTRIBUTION / AVAILABILITY STATEMENT Approved for public release; distribution is unlimited		12b. DISTRIBUTION CODE
13. ABSTRACT (maximum 200 words)		
<p>It is widely published that the terahertz (THz) spectral range has potential for imaging in the fields of military and security applications. The Sensors Research Laboratory previously achieved real-time imaging of concealed objects using a 1mW quantum cascade laser (QCL) and an uncooled vanadium oxide/silicon nitride based microbolometer. This thesis introduces an amorphous silicon based microbolometer with improved NETD in the 8-12 μ m infrared spectral range. The QCL is usually operated in pulsed mode with rate in the hundreds of kHz which is much higher than the cut-off frequency of microbolometers of about tens of Hz. This indicates that neither camera should be able to detect the individual pulses of the THz beam. A detailed analysis showed that microbolometers can only detect the average power. Earlier experiments were then reproduced using the amorphous silicon based camera to assess the image quality but found it to be inferior to the silicon nitride based camera. These observations indicate that the absorption of THz in amorphous silicon is much weaker than silicon nitride. Other materials used to conceal military assets were analyzed and imaged to prove in principal the possibility of active THz imaging detection at a distance in narrow atmospheric windows.</p>		

14. SUBJECT TERMS THz, microbolometer, uncooled, quantum cascade laser, imaging, detection, camera, NETD.		15. NUMBER OF PAGES 72
		16. PRICE CODE
17. SECURITY CLASSIFICATION OF REPORT Unclassified	18. SECURITY CLASSIFICATION OF THIS PAGE Unclassified	19. SECURITY CLASSIFICATION OF ABSTRACT Unclassified
		20. LIMITATION OF ABSTRACT UU

NSN 7540-01-280-5500

 Standard Form 298 (Rev. 2-89)
 Prescribed by ANSI Std. Z39-18

THIS PAGE INTENTIONALLY LEFT BLANK

Approved for public release; distribution is unlimited

**REAL TIME IMAGING ANALYSIS USING A TERAHERTZ QUANTUM
CASCADE LASER AND A MICROBOLOMETER FOCAL PLANE ARRAY**

Kevin William Buchanan
Major, Canadian Army
BSc., Royal Military College of Canada, 1995

Submitted in partial fulfillment of the
requirements for the degree of

MASTER OF SCIENCE IN APPLIED PHYSICS

from the

**NAVAL POSTGRADUATE SCHOOL
December 2008**

Author: Kevin William Buchanan

Approved by: Gamani Karunasiri
Thesis Advisor

Scott Davis
Co-Advisor

James H. Luscombe
Chairman, Department of Physics

THIS PAGE INTENTIONALLY LEFT BLANK

ABSTRACT

It is widely published that the terahertz (THz) spectral range has potential for imaging in the fields of military and security applications. The Sensors Research Laboratory previously achieved real-time imaging of concealed objects using a 1mW quantum cascade laser (QCL) and an uncooled vanadium oxide/silicon nitride based microbolometer. This thesis introduces an amorphous silicon based microbolometer with improved NETD in the 8-12 μm infrared spectral range. The QCL is usually operated in pulsed mode with rate in the hundreds of kHz which is much higher than the cut-off frequency of microbolometers of about tens of Hz. This indicates that neither camera should be able to detect the individual pulses of the THz beam. A detailed analysis showed that microbolometers can only detect the average power. Earlier experiments were then reproduced using the amorphous silicon based camera to assess the image quality but found it to be inferior to the silicon nitride based camera. These observations indicate that the absorption of THz in amorphous silicon is much weaker than silicon nitride. Other materials used to conceal military assets were analyzed and imaged to prove in principal the possibility of active THz imaging detection at a distance in narrow atmospheric windows.

THIS PAGE INTENTIONALLY LEFT BLANK

TABLE OF CONTENTS

I.	INTRODUCTION.....	1
II.	BACKGROUND	3
	A. IMAGING USING TERAHERTZ SOURCES.....	3
	B. INFRARED CAMERAS	5
	C. EARLY EXPERIMENTATION AFFECTS RESEARCH DIRECTION	6
	D. RESEARCH OBJECTIVES.....	7
III.	THEORY - SOURCE, DETECTOR AND PROPOGATION MEDIUM	9
	A. THZ SOURCE - QUANTUM CASCADE LASERS	9
	1. Quantum Cascade Laser Theory.....	10
	2. 2.8 and 3.6 THz QCLs	11
	3. 2.8 and 3.6 THz QCL Performance.....	11
	B. DETECTOR - MICROBOLOMETER	15
	1. Microbolometer Theory	15
	2. Analysis of Microbolometer Operation under Pulsed Power	18
	3. Responsivity \mathcal{R}	22
	4. Noise Equivalent Temperature Difference (NETD)	23
	C. THZ TRANSMISSION IN THE ATMOSPHERE AND MATERIALS ..	26
	1. Atmospheric Transmission	26
	2. THz Laser Beam Propagation	29
	3. FPAs, Optical Components (Tsurupica) and Plastic Tape	30
	4. Camouflage and Suppression of Military Assets	32
IV.	EXPERIMENTAL SET UP AND THZ IMAGING	33
	A. OPTIMIZATION OF QCL POWER	33
	B. OPTIMIZED IMAGING ARRANGEMENT	35
V.	RESULTS	37
	A. OPTIMIZATION OF QCL PERFORMANCE	37
	B. ANALYSIS OF CAMOUFLAGE MATERIALS	40
	C. PERFORMANCE OF TWO CAMERAS AND THZ IMAGING	45
VI.	CONCLUSIONS	49
	LIST OF REFERENCES	53
	INITIAL DISTRIBUTION LIST	57

THIS PAGE INTENTIONALLY LEFT BLANK

LIST OF FIGURES

Figure 1.	THz imaging arrangement. THz QCL is housed in a cryostat with emerging divergent beam collimated with parabolic mirrors passing through an object, and then focused onto a microbolometer focal plane array (from [18]).	3
Figure 2.	2.8 THz imaging of utility knife wrapped in tape shown in (a). (b) Single frame image produced by IR-160 camera. (c) 50 frame average. (d) 50 frame composite image (from [17]).	4
Figure 3.	Infrared Solutions, Inc. IR-160 thermal imaging camera (from [23]).	5
Figure 4.	Schematic of an individual pixel from Infrared Solutions, Inc. IR-160 thermal imaging camera (from [34]).	5
Figure 5.	Thermoteknix Systems Ltd. Miricle 110K model thermal imaging camera (from [24]).	6
Figure 6.	QCL band structure (from [10]).	10
Figure 7.	(a) Band structure and (b) waveguide of bound-to-continuum 3.6 THz QCL used in this experiment (from [10]).	11
Figure 8.	(a) I-V analysis for the 3.6 THz QCL operated under 5, 10, 15, 20, and 25% duty cycles. (b) I-V analysis for the 3.6 THz QCL operated at 10% duty cycle for cryostat temperatures ranging from 0 K to 100 K (from [18]).	13
Figure 9.	(a) Peak power analysis for the 3.6 THz QCL, operated under 5, 10, 15, 20, and 25% duty cycles and (b) peak power analysis for the 3.6 THz QCL, operated under 10, 15, 20, and 25% duty cycles over time (from [18]).	14
Figure 10.	Schematic of a typical microbolometer pixel structure (from [34]).	16
Figure 11.	Modulated radiation incident on focal plane array.	17
Figure 12.	Temperature change in a pixel for $P_0 = 1.25$ mW, $\eta = 0.64$, $G = 10^{-7}$ W/K and $\tau = 10$ ms. Response of second term in Equation 1.14 (solid line) compared to average power term (dashed line)	20
Figure 13.	(a) RC circuit used to model equation 1.16. (b) 300 Hz PRF and (b) 300 kHz PRF.	21
Figure 14.	Spectral Radiance of a blackbody at 300K (from [16]).	24
Figure 15.	FASCODE model of atmospheric loss at sea level on a clear day.	27
Figure 16.	FASCODE model of atmospheric loss for a) 2.8 and b) 3.6 THz windows.	27
Figure 17.	a) HITRAN model and FTIR results of atmospheric loss for b) 4.3 and c) 4.9 THz windows. HITRAN (solid line) and FTIR results (dashed line). Lasing spectra of QCL's are depicted with dashed vertical lines (from [14]).	28
Figure 18.	FASCODE model of atmospheric loss for a) 4.3 and b) 4.9 THz windows.	28
Figure 19.	Maximum propagation distance for 200 mW 4.9 THz QCL using FTIR measured, FASCODE modeled and HITRAN modeled extinction coefficients.	29
Figure 20.	Percent absorption of FPAs. (a) SiN and (b) Si (after [41]).	30

Figure 21.	Percent transmission of (a) Tsurupica 4.0 mm, and (b) polytape 0.25 mm.....	31
Figure 22.	3.6 THz QCL mounted on copper thermal dissipation block attached to cold finger. Red arrow in inset depicts direction of laser output beam. Shroud has been removed from the CCR system (from [16]).	33
Figure 23.	Schematics of the optics used in THz imaging.....	35
Figure 24.	(a) Peak power of the device given a pulse generator impedance 50Ω into $5, 10, 15$ and 20Ω at various frequencies, and (b) peak power of the device at 100 kHz given a pulse generator impedance of 50Ω into 11 to 15Ω	37
Figure 25.	(a) Peak power of the device given a 10% duty cycle, and a pulse generator impedance of 50Ω into 13Ω for various currents and pulse frequencies, and (b) peak power of the device given a 10% duty cycle, and a pulse generator impedance of 50Ω into 13Ω or with transformer for various currents and PRF of 100 and 300 kHz.....	38
Figure 26.	(a) Peak power of the device at 100 kHz for 10 and 20% duty cycles, with a pulse generator impedance of 50Ω into 13Ω at various currents, and (b) peak power of the device given a 10% duty cycle, with a pulse generator impedance of 50Ω into 13Ω at various frequencies after 1 and 5 minutes of lasing.....	39
Figure 27.	(a) 2.8 THz QCL peak power given a 10% duty cycle, and a pulse generator impedance of 50Ω into 3 to 7Ω , and (b) peak power given a 10% duty cycle, and a pulse generator impedance of 50Ω into 5Ω for various currents and PRFs.	39
Figure 28.	a) I-V characteristics and peak power output of the 3.6 THz QCL given a 10% duty cycle, with a pulse generator impedance of 50Ω into 13Ω at a PRF of 100 kHz, and b) I-V characteristics and peak power output of the 2.8 THz QCL given a 10% duty cycle, with a pulse generator impedance of 50Ω into 5Ω at a PRF of 100 kHz.	40
Figure 29.	a) Photographs of combat uniform, arid region (top), 0.32 mm, and temperate woodland (bottom), 0.32 mm, and b) percent transmission of arid region combat uniform.	41
Figure 30.	a) Photograph of temperate woodland camouflage screen, black and green garnish, 0.49 mm, and b) percent transmission of temperate woodland camouflage screen.	41
Figure 31.	a) Photograph of winter operations camouflage screen, 1.12 mm, and b) percent transmission of winter operations camouflage screen.	42
Figure 32.	(a) Photographs of thermal blankets, temperate woodland (top left), arid (top right) and winter operations (bottom center), and (b) typical percent transmission for all samples.	42
Figure 33.	a) Photograph of heat transfer reduction system without insulating layer, base layer (right) and scrim (left), and b) percent transmission of heat transfer reduction system, base layer and scrim.	43
Figure 34.	a) Photograph of woodland vehicle camouflage net, and b) percent transmission of garnish.	44

Figure 35.	a) Photograph of the arid region mobile camouflage system, base layer (left) and scrim (right) and b) percent transmission of scrim only	44
Figure 36.	a) Picture of winter operations mobile camouflage system, garnish, backing layer, base layer, and garnish, and b) percent transmission base layer only	45
Figure 37.	a) Photograph of the imaging setup (from [16]), b) IR image of (a) using Miricle 110K camera, and b) IR image of (a) using IR-160 camera.	45
Figure 38.	a) Background using Infrared Solution IR-160 camera, b) 2.8 THz beam using 50Ω into 5Ω at a PRF of 100 kHz, 20% Duty Cycle, c) background using Thermoteknix Miricle 110K camera and d) 2.7 THz beam using 50Ω into 5Ω at PRF 100 kHz.	46
Figure 39.	a) Knife concealed by plastic tape, b) 2.8 THz image using Infrared Solution IR-160 infrared microbolometer camera and c) 3.6 THz image using Infrared Solution IR-160 infrared microbolometer camera	47
Figure 40.	a) 2.8 THz beam, b) Un-obsured knife, and c) Knife obscured with tape.....	47
Figure 41.	a) 2.8 THz beam, b) un-obsured knife and c) knife obscured with tape....	48
Figure 42.	Knife covered with woodland camouflage net a) camouflage net coming into beam, b) covered knife coming into beam, c) covered knife fully visible in beam.	48

THIS PAGE INTENTIONALLY LEFT BLANK

ACKNOWLEDGMENTS

The author would like to thank the Canadian Forces, and the Electrical Mechanical Engineering Branch for providing me the opportunity to study at the Naval Postgraduate School. I would also like to thank the physics department professors and support staff at NPS, for both the quality education I received, and the friendships developed while there. Most importantly I would like to thank my thesis advisors Professors Gamani Karunasiri and Scott Davis for their ideas, input and patience during my research time at NPS. Finally to my family, Natasha, Jaden and Finley, it's time to make up for lost time. Your support is what really kept me going.

I. INTRODUCTION

In the days following the September 11, 2001 attacks on the United States the world security and threat environments changed drastically. Paralleling the political response was a push for technological solutions to address vulnerabilities that had been exploited by the attackers. Solutions included technologies leveraging our existing usage of the electromagnetic spectrum for security screening. Few of these threats were effectively countered, and new technological developments continued to be sought. One technology being considered was terahertz (THz) radiation, 0.3 to 10 THz, and in particular, THz imaging as a means of detecting hidden objects concealed by clothing. In 2003 practical employment of such a system was far from being realized, and early papers exploring the topic were limited to proof-of-principle experiments promoting the potential of using non ionizing radiation with submillimeter resolution to perform security screening [1]. The principals were sound, and research into the use of THz radiation for security purposes quickly grew to encompass possibilities for detecting weapons of mass destruction and mine field detection through a combination of far IR spectroscopy and THz imaging [2]-[4]. By 2005, research in this area of THz detection of weapons and explosives was still largely theoretical [5], but papers analyzing THz transmission through various materials like common clothing and optical components continued to support its probable realization [7]-[8]. Experimental research was slow to evolve largely to a lack of THz sources and effective detectors for imaging and not from limited potential [9]. One research area developing between 2004 and 2006 involved the use of a quantum cascade laser (QCL) as a THz source in a THz imaging arrangement with a micrololometer camera as the detector [10]-[15]. The Sensors Research Laboratory (SRL) at the Naval Postgraduate School began THz imaging experimentation in this timeframe and advanced the pioneering work done at Agilent Laboratories in Santa Clara. Since that time, the SRL has contributed four research papers to the field, and the research reported in this thesis builds on that foundation [15]-[18].

THIS PAGE INTENTIONALLY LEFT BLANK

II. BACKGROUND

A. IMAGING USING TERAHERTZ SOURCES

THz imaging using QCL's holds significant promise for security and screening applications, largely due to its high average power, non-ionizing radiation and sub-mm spatial resolution. Early imaging work [10]-[15] provided meager results, but THz technology has continued to attract attention with advances in photonics and nanotechnology [19]-[20]. QCL performance was once a limiting factor, but THz QCL's can now operate at room temperature [21] and at power levels in the tens of mW's [19]-[22]. The Sensors Research Laboratory, headed by Professor Gamani Karunasiri, has made contributions to the field of THz imaging using uncooled microbolometer cameras as detectors and QCL's as sources. Some significant images and videos published in scientific literature have come from LCol Barry Behnken and Professor Karunasiri. These can be seen in two papers titled "Real-time imaging using a 2.8 THz quantum cascade laser and uncooled infrared microbolometer camera" [17] and "Optimization of a 3.6-THz Quantum Cascade Laser for Real-Time Imaging with a Microbolometer Focal Plane Array" [18]. An example of these images and the imaging arrangement can be seen in Figure 1 [18] and Figure 2 [17].

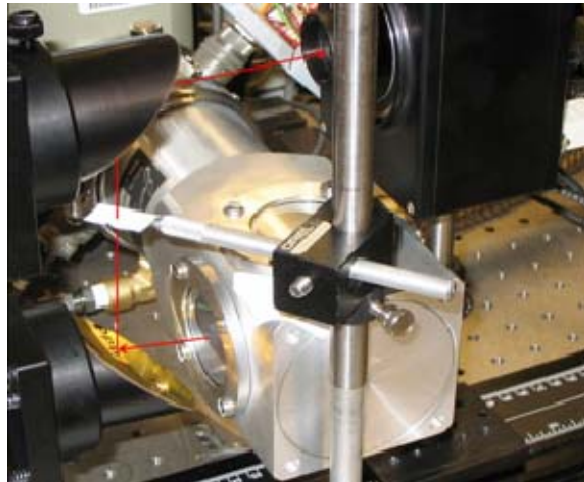


Figure 1. THz imaging arrangement. THz QCL is housed in a cryostat with emerging divergent beam collimated with parabolic mirrors passing through an object, and then focused onto a microbolometer focal plane array (from [18]).

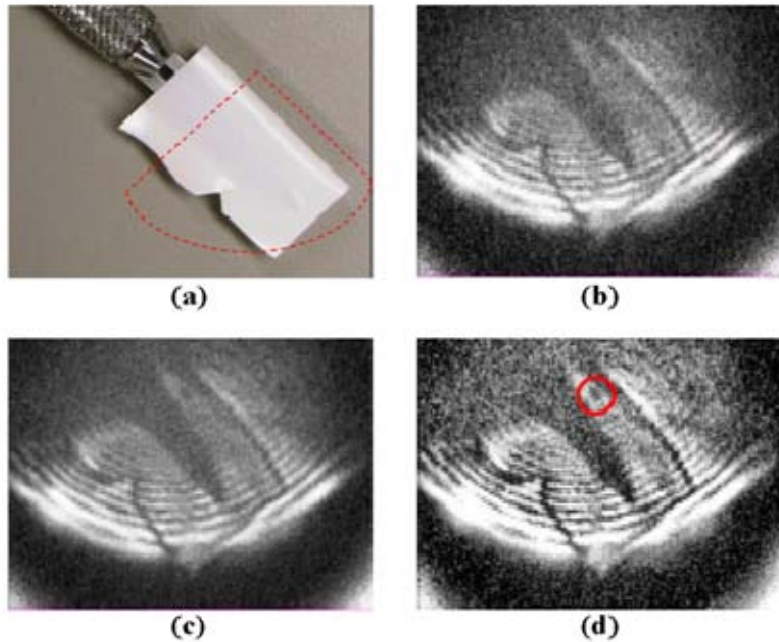


Figure 2. 2.8 THz imaging of utility knife wrapped in tape shown in (a). (b) Single frame image produced by IR-160 camera. (c) 50 frame average. (d) 50 frame composite image (from [17]).

The images were produced by an optically modified microbolometer camera, the IR-160 by Infrared Solutions. The significance of this work is that a very low powered (1mW) QCL has enabled imaging of a knife blade concealed in tape, the closest any research has come to realizing the highly touted potential introduced earlier.

Where that research ended is essentially where this thesis research began. In an attempt to improve the imaging quality of our experimental set-up, other contributions to the field were studied. Most notable was a paper titled "Real Time Imaging Using a 4.3-THz Quantum Cascade Laser and a 320x240 Microbolometer Focal Plane Array" written by Alan Lee at the Massachusetts Institute of Technology [12]. That research group improved their results by synchronously modulating the QCL and bolometer focal plane array, thereby allowing differential imaging and reducing 1/f noise. This thesis research initially set out to accomplish differential imaging employing our pre-existing set-up. To do this a newer, more responsive digital vice analog camera was incorporated in the apparatus. The original and newer cameras are described in detail below.

B. INFRARED CAMERAS

The camera used in the previous experiments [15]-[18] was an Infrared Solutions IR-160 un-cooled microbolometer camera [23]. The camera is pictured in Figure 3.



Figure 3. Infrared Solutions, Inc. IR-160 thermal imaging camera (from [23]).

The focal plane array (FPA) consists of 160x120 pixels with a pitch of $50\mu\text{m}$ each. The FPA is comprised of a vanadium oxide (VO_x) film applied to a silicon nitride (Si_3N_4) membrane. This active layer is attached via support legs to a Si_3N_4 substrate that acts as a heat sink. The structure can be seen in Figure 4.

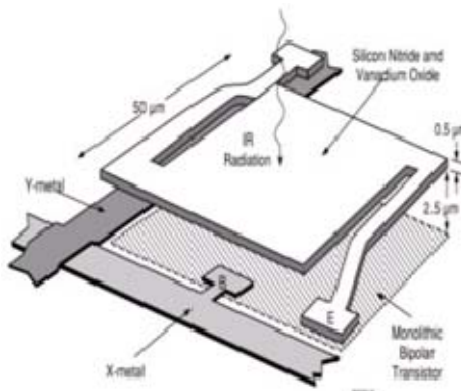


Figure 4. Schematic of an individual pixel from Infrared Solutions, Inc. IR-160 thermal imaging camera (from[34]).

The thermal response time is 10 ms, and the temperature coefficient of resistance (TCR) is -0.023 K^{-1} . The camera has a 30 Hz frame rate and is designed to operate in the 8 to 14 μm spectral range with a noise equivalent temperature difference (NETD) of $<100\text{ mK}$. The optics used in the IR regime is a 20 mm focal length, f/0.8 germanium lens with antireflective coating. The modified optics consisted of a f/1 Tsurupica lens with no antireflective coating.

The second camera, pictured in Figure 5, is a Miricle 110K uncooled microbolometer made by Thermoteknix Inc [24].



Figure 5. Thermoteknix Systems Ltd. Miricle 110K model thermal imaging camera (from [24]).

Its FPA consists of 384x288 pixels, each with a pitch of 35 μm . The active and substrate layers are amorphous silicon with a thermal response time of 7 ms and TCR of $-0.02\text{ }^{\circ}\text{C}^{-1}$. The camera operates at a frame rate of 50 to 60 Hz and is designed for the 7-14 μm , spectral region with a NETD of $<50\text{ mK}$. The optics used in the IR regime is a 25 mm, f/1 germanium lens with antireflective coating. The modified optics consisted of a f/1 Tsurupica lens with no antireflective coating. The camera also offers an external sync mode that allows synchronization of the camera with an external signal. This feature was necessary for experiments utilizing a differential imaging scheme.

C. EARLY EXPERIMENTATION AFFECTS RESEARCH DIRECTION

Early experiments conducted by simply swapping out the original camera failed to produce any images at all, let alone improved images. This directly prevented us from

achieving our original goals and heavily influenced the direction the thesis research took. The arrangement had to be re-analyzed, and the source was considered first. Previous experiments assumed that the best operating frequency was 300 kHz and that impedances were correctly matched. Careful analysis showed that there was an impedance mismatch affecting the output. The procedure for determining the best operating parameters for thermal imaging were developed using a 3.6 THz QCL and 2.8 THz QCL. This was the first major experiment undertaken. The results are reported in the following chapters. This still failed to yield improved results, and, in fact, the results were marginal compared to any of the previous work. Hoping to find answers in the theory, a careful review revealed that the theory presented in earlier work predicted that we should not be able to see an image at all given the optical power of the QCL. A theory was developed that adequately explained why we should be able to see images as demonstrated in previous research, but it did not explain the poor image quality then being attained. The cameras were then compared directly with each other, with surprising results. In spite of the much lower NETD for the new camera, <50 mK vice <100 mK, it produced very faint images when compared to the original camera, even with an identical beam and, identical optical components. This led to the idea that, although the NETD predicted better performance in the 7 to 14 μ m range, the focal planes were different materials and perhaps they were responsible for the unpredictable results. The absorption characteristics of the focal plane arrays were then analyzed at THz frequencies and found to predict the bolometer output. The development of a plausible theory explaining why we are able to image at THz frequencies and the discovery of the significantly different focal plane responses at THz frequencies from IR wavelengths became the major focus of this thesis research.

D. RESEARCH OBJECTIVES

The objectives of this thesis research are as follows:

1. Present a theory that adequately explains why we are able to see an image illuminated by a THz QCL using an optically modified un-cooled microbolometer.

Failures in the existing theory will also be presented through a careful analysis of thermal imaging device figures-of-merit, namely responsivity, noise equivalent power and noise equivalent temperature difference.

2. Develop a method for optimizing QCL operation for use in THz imaging. Report results for impedance matching and frequency selection of the applied signal to yield the highest possible optical power output. Using the optimized operating parameters, investigate and report the laser IV characteristics for a 2.8 and 3.6THz QCL.
3. Investigate THz propagation through optical components, material shown to be of interest in previous research and material of military significance presented in this thesis. Report results of proof-of-principle experiment as to whether THz imaging holds any promise for battlefield sensing.
4. Demonstrate the performance of the IR-160 and Miricle 110K infrared microbolometer cameras in a THz imaging role. Contrast the performance of the two cameras in the IR regime, and show how the FPA material is responsible for the altered performance in the THz regime. Show how the FPA material also accounts for altered image quality at different THz frequencies. Make recommendations for an improved THz sensor based on this.

III. THEORY - SOURCE, DETECTOR AND PROPOGATION MEDIUM

A. THZ SOURCE - QUANTUM CASCADE LASERS

The idea behind quantum cascade lasers (QCL) was first proposed by Kazarnov and Souris in 1971, published in a paper titled "Possibility of amplification of electromagnetic waves in a semiconductor with a superlattice," [25]. Although QCLs are based on semiconductors, the theoretical laser contrasts sharply to that of semiconductor lasers. Semiconductor lasers rely on electron hole recombination or interband transitions to emit photons. In bipolar semiconductor devices the photon wavelength is determined by this irraditative recombination across a band gap in the active layer of a forward-biased pn junction [26]. In contrast to this, the QCL is a unipolar device that uses a quantum well (QW) structure to emit photons when an electron undergoes an intraband transition within the well. When a voltage is applied to a series of spaced QWs, the electron can be made to "cascade" from one QW to a lower potential QW by consecutive tunneling, emitting a photon with each cascade. Implementation of practical QCLs has allowed lasers to operate at frequencies that are impossible with bipolar junction lasers, due to the extremely small band gaps required, and complications arising from thermal repopulation. The first QCL was produced at Bell Labs in 1994 by J. Faist et al [26]. Since then, QCLs have become the dominant mid-infrared semiconductor laser technology. In 2001 a laser with energy less than optical phonon energy was demonstrated at $67\text{ }\mu\text{m}$, or 4.4 THz [27]. Selection of QW width and spacing, and advances in molecular beam epitaxy (MBE) fabrication techniques allowed the QCL to have a lasing frequency tailored by design, which has allowed operation to extend into the THz regime [22]. Steady advances from 2001 to today include: continuous wave (CW) operation at THz frequencies [28], low threshold currents [29], and high optical power with minimal cooling at THz frequencies [30]-[31]. This has opened up a world of possibilities for applications in numerous fields and has directly contributed to the advancement of THz imaging.

1. Quantum Cascade Laser Theory

The key feature that distinguishes the QCL from other semiconductor lasers is the intersubband transition. A simple QCL model is a three level laser, with states $|3\rangle$, $|2\rangle$, and $|1\rangle$. Figure 6 shows how electrons are injected into the level $|3\rangle$ via the miniband in the left supperlattice barrier. The electrons that are unable to tunnel into the continuum via the minigap on the right fall to the level $|2\rangle$ by emitting a photon.

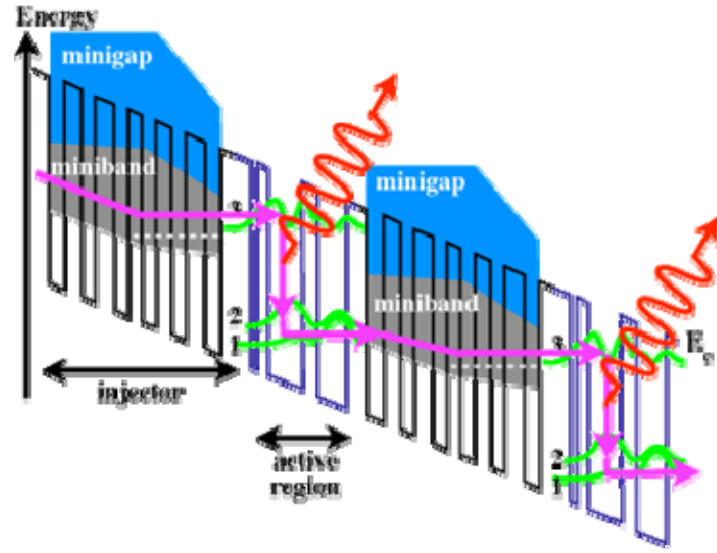


Figure 6. QCL band structure (from [10]).

The population inversion required for gain is created by the lifetime τ_{32} being significantly longer then the lifetime τ_{21} . To achieve this, the lifetime τ_{32} for a level $|3\rangle \rightarrow |2\rangle$ transition is prolonged due to the significant momentum transfer that must occur, and the lifetime τ_{21} for a level $|2\rangle \rightarrow |1\rangle$ transition is reduced by making it resonant with the optical phonon energy of the host semiconductor. The resulting power achieved is the same as that for a conventional laser but with the addition of N active regions in the multiple quantum well (MQW) structure as seen in equation 1.1 [32].

$$P_{\text{out}} = \eta_{\text{ext}} N \frac{h\nu}{q} (I - I_{\text{threshold}}) \quad (0.1)$$

2. 2.8 and 3.6 THz QCLs

The lasers used in our imaging experiments are a bound-to-continuum design optimized for 2.8 and 3.6 THz operation. The epitaxial MQW layers consist of $\text{Al}_{0.15}\text{Ga}_{0.85}\text{As}$ and GaAs with 120 periods for the 3.6 THz laser and 120 for the 2.8 THz laser. The band diagram and layer widths (in nanometers) of the quantum wells are shown in Figure 7, with the GaAs layers highlighted in bold characters.

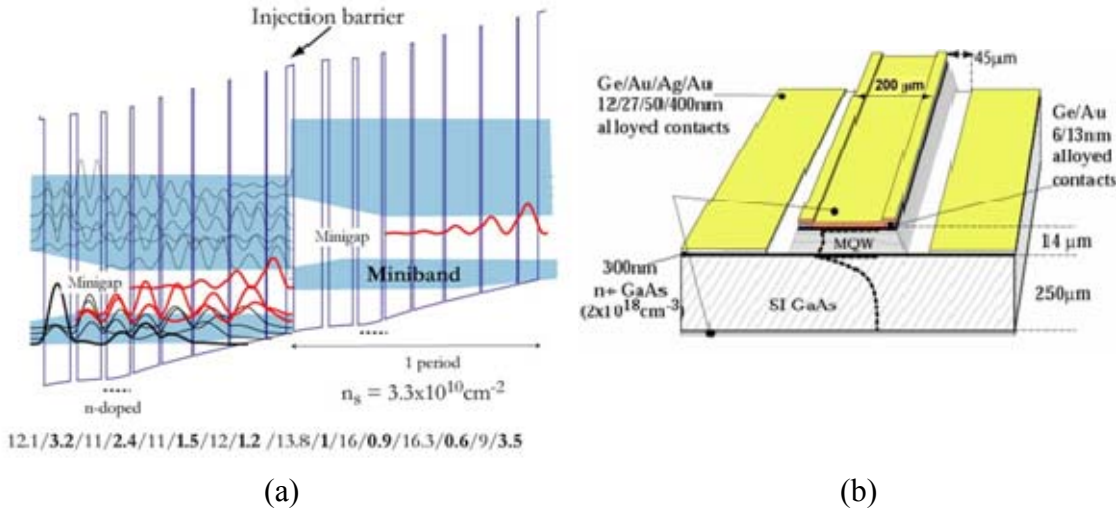


Figure 7. (a) Band structure and (b) waveguide of bound-to-continuum 3.6 THz QCL used in this experiment (from [10]).

It is very evident from Figure 7 that, if the applied bias is not correct, it is very likely that electrons will not tunnel into their intended energy state and that the device will not function as intended. This will seriously deteriorate the performance characteristic we are most interested in, the optical power output. The device must be cooled to approximately 10 K to reduce thermal excitation of electrons, and it heats up significantly with the necessary applied currents of close to 1 A. Characterization of THz QCL performance for optical imaging purposes must consider all these factors. They are discussed in detail below.

3. 2.8 and 3.6 THz QCL Performance

There are a number of factors that contribute to the performance of a QCL. Band misalignment and power reduction can occur from an improperly applied bias, impedance

mismatch between power supply, and laser as well as thermal effects. Thermal effects are mitigated through cryogenic cooling and pulsed mode operation, while the device's dynamic impedance can only be determined experimentally through I-V measurement. The lasers used in this research were analyzed in previous works authored by NPS students. The first analysis concentrated on the impedance issues involved in optimizing power output [15], while the others analyzed effects related to both the pulse duty cycle and the operating temperature [16]-[18].

An assignment of unique impedance characteristic for the device is difficult due to the dynamic nature of its operation. It does not have a conventional "operating point". The 3.6 THz QCL impedance was previously reported as 3.47Ω by Agilent Laboratories [10]. The SRL constructed a step-down transformer using this information to match the known 50Ω characteristic impedance of coaxial cables [15]. The transformer turns ratio appropriate to the device was calculated by considering the transfer characteristics. The power (P_{in}) to the primary windings of a transformer and the power (P_{out}) out of the secondary windings must be matched for optimal power transfer between source and load. Since the power can be expressed as $P=IV$ or $P=I^2Z$ where I is current, V is the voltage and Z is the impedance it follows that $Z_{in}I_{in}^2 = Z_{out}I_{out}^2$. It should be noted that power losses are reduced when current is reduced. The induced EMF (ξ_{turn}) is the same in the primary and secondary windings, allowing it to be expressed as $\xi_{turn} = V_p/N_p = V_s/N_s$ where V_s and V_p are the voltages in the secondary and primary windings, and N_s and N_p are the number of windings in the secondary and primary windings. This can all be expressed in the following equation.

$$Z_{out} = Z_{in} \left(\frac{N_p}{N_s} \right)^2 \quad (0.2)$$

The transformer constructed used the turns ratio $(N_p/N_s)^2 = 0.26$, based on the laser's reported 3.47Ω impedance. Follow-on work reported by the SRL [16]-[18] used this transformer and determined that the impedance was dynamic and depended on cryostat temperature and duty cycle, but, despite these variations, this transformer was ultimately used for both the 2.8 and 3.6 THz QCLs.

The duty cycle can have an effect on both the device temperature and the device impedance. This can be seen in Figure 8, where the I-V characteristics for this device were measured at a 300 kHz pulse repetition frequency and over 5%-25% duty cycles.

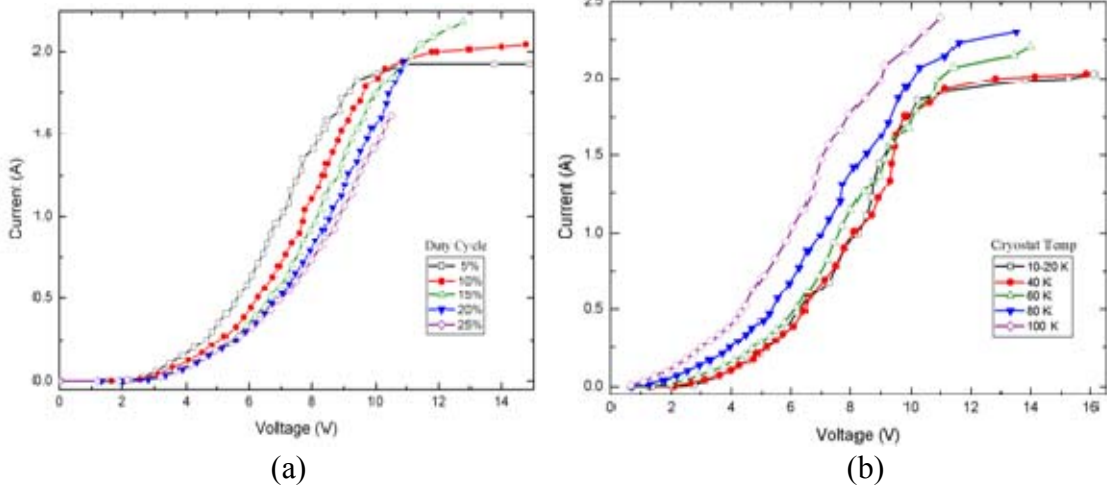


Figure 8. (a) I-V analysis for the 3.6 THz QCL operated under 5, 10, 15, 20, and 25% duty cycles. (b) I-V analysis for the 3.6 THz QCL operated at 10% duty cycle for cryostat temperatures ranging from 0 K to 100 K (from [18]).

The impedance was measured to be 2.7Ω [18], which differs substantially from that reported in Reference [10]. Finally, the cryostat temperature can affect the dynamic impedance. This can be seen in Figure 8, where the I-V characteristics for this device were measured at a 300 kHz pulse repetition frequency with a 10% duty cycle and over a temperature range of 0 K-100 K. The dynamic impedance can clearly be seen to be changing again in this analysis. Optimized QCL performance for this laser clearly has to focus on narrowing the dynamic impedance to that corresponding to peak THz power output, the region where optimal imaging would occur.

The performance optimization in reference [18] focused on analyzing the duty cycle for peak output power. Figure 9 shows how the duty cycle affects the peak output power as measured by a FTIR for duty cycles of 5, 10, 15, 20, and 25% .

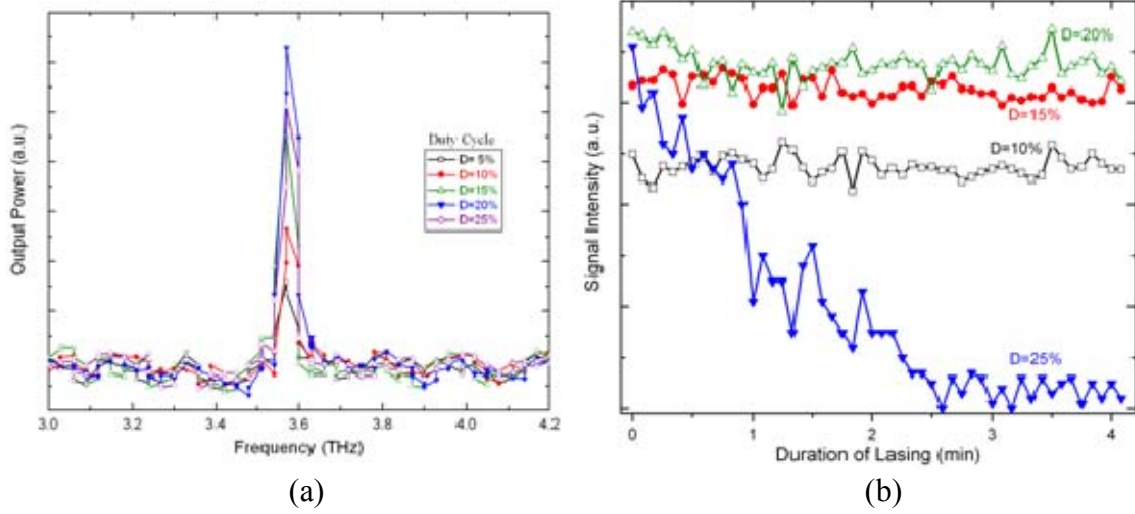


Figure 9. (a) Peak power analysis for the 3.6 THz QCL, operated under 5, 10, 15, 20, and 25% duty cycles and (b) peak power analysis for the 3.6 THz QCL, operated under 10, 15, 20, and 25% duty cycles over time (from [18]).

The peak power was delivered with a 20% duty cycle upon initial start up of the laser cooled to 10 K. The cryostat temperature, and therefore device temperature, was affected by the duty cycle. The temperature change was then shown to have an effect on the signal intensity. Over a 4 minute lasing interval the signal intensity would degrade. The best operating duty cycle maximized the power applied to the detector while minimizing Joule heating of the device. Figure 9 clearly shows this optimization occurring at 20%. A 15% duty cycle did not put as much power on the detector, but at 25% heated up the device's temperature increased significantly through Joule heating, which degraded the output.

In all of the above analyses, a 300 kHz pulse rate was employed, and the transformer described earlier was used. As it applies to this project, the results of the 20% duty cycle output power optimization was consistently used, but all other assumptions about the optimal frequency, proper dynamic impedance range and transformer construction were not. These issues are addressed in the experimental procedure, section IV, and were a new method for determining the best operating parameters for both the 2.8 and 3.6 THz QCLs were developed.

B. DETECTOR - MICROBOLOMETER

Uncooled microbolometer focal plane arrays (FPAs) for thermal imaging were first developed in 1983 by Honeywell using silicon micromachining and the well known dependence of material resistance on temperature (bolometric effect). The project was funded by both the US Army Night Vision Laboratories and the Defense Advanced Research Projects Agency. In 1989 they made a device consisting of 64 x 128 pixels consisting of silicon nitride (SiN) membranes and vanadium oxide (VO_x) resistive film with a temperature coefficient of resistance (TCR) of approximately 2% per $^{\circ}C$. The detector was attached to a monolithic read out integrated circuit [33]. Since then, uncooled solid state infrared imaging arrays have continued to advance with material and micromachining breakthroughs. Although microbolometers FPAs of this type were developed primarily for infrared imaging, the bolometric effect is responsive across the entire electromagnetic spectrum. These devices can therefore be used to detect radiation at all wavelengths and, in particular, have applications in terahertz imaging.

The figures-of-merit typically used to quantify the performance of infrared microbolometers can be adopted to quantify the device performance in the terahertz spectrum as the devices are adapted for use in this regime.

1. Microbolometer Theory

As mentioned above, a microbolometer is a thermal detection device that uses heat flow to affect a measurable quantity in a sensing element. The radiant power P_o incident on the detector causes the sensing element to undergo a temperature increase proportional to the heat absorbed by the pixel at that particular position in the array. In the case of a microbolometer, this temperature change ΔT causes a change in resistance ΔR . If the absorbed radiation is small, this change is linear with the incident power [34]. The degree with which this effect is felt is quantified by the TCR, α , and the device resistance R . This is expressed as

$$\Delta R = \alpha R \Delta T. \quad (0.3)$$

Figure 10 shows schematic of a typical microbolometer pixel structure with a thin film vanadium oxide (VO_x) resistive sensing element.

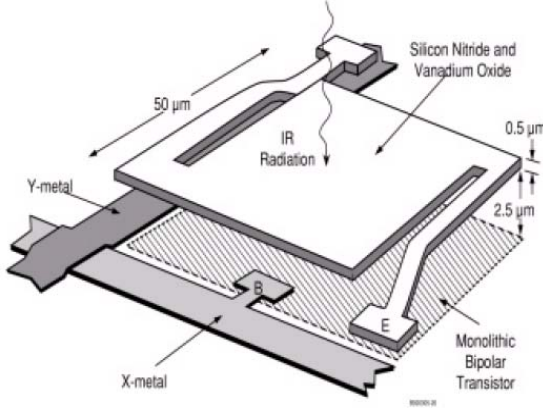


Figure 10. Schematic of a typical microbolometer pixel structure (from [34]).

Proper thermal isolation of these structures prevents leakage conduction to neighboring pixels and convection losses to the surrounding atmosphere. In the ideal case, the temperature change on the sensing area is followed by heat flow down the support legs to the substrate. If the sensing area has a heat capacity C (J/K) the relation between the heat Q the element absorbs with a temperature change ΔT is $Q = C\Delta T$. The change with respect to time is therefore $dQ/dt = C(d\Delta T/dt)$. As the temperature of the element rises, with respect to the substrate, heat conduction begins. The absorbed thermal energy is then lost through the support structure. This loss is characterized by a thermal conductance G (W/K), and it occurs at a rate $G\Delta T$. When radiative power P_o is incident on the sensing area, assuming that the device remains approximately in thermodynamic equilibrium, the heat balance equation can be expressed as

$$P_o = G\Delta T + C \frac{d\Delta T}{dt}. \quad (0.4)$$

In practice, it is desirable to modulate the incident radiation beam, in order to employ standard noise-minimization techniques such as synchronous detection (lock-in methods), dynamic averaging (boxcar integration), 1/f noise suppression, and so forth. Hence, P_o is deliberately forced to be an explicit function of time, $P_o(t)$. The solution of equation 1.4 may then be expressed as a time-shifted linear superposition of the detector's impulse response (Green's function), which is exponential with a characteristic time constant τ [34]-[35]. This can be seen in Figure 11.

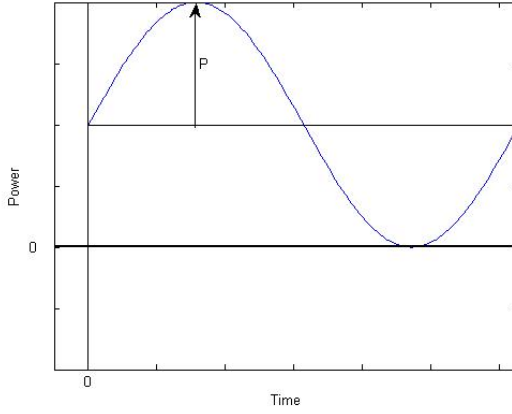


Figure 11. Modulated radiation incident on focal plane array.

When modulated radiation power $P_0 e^{j\omega t}$ is incident on the sensing area with absorption efficiency η , neglecting average power, the heat balance equation can now be expressed as

$$\eta P_0 e^{j\omega t} = G\Delta T + C \frac{d\Delta T}{dt}. \quad (0.5)$$

By assuming a Green's function of the form $e^{\tau/t}$, where the thermal time constant $\tau = C/G$, we can solve the above equation as follows:

$$\int \frac{d}{dt} \Delta T e^{\tau/t} dt = \frac{\eta P_0}{C} \int e^{(1/\tau + j\omega)t} dt. \quad (0.6)$$

As time goes to infinity, or in the steady state, the result is

$$\Delta T = \text{Re} \left[\frac{\eta P_0 e^{j\omega t}}{(G + j\omega C) e^{j\phi}} \right], \quad (0.7)$$

where $\tan(\phi) = \omega\tau$. This result can be recast as [35]

$$\Delta T = \frac{\eta P_0}{G\sqrt{1 + \omega^2\tau^2}} \sin(\omega t - \phi). \quad (0.8)$$

From this we can gain an idea of how a pixel should respond when operated within the context of pulse-modulated terahertz imaging. If we assume a pixel to be thermally isolated, with typical thermal parameters $C = 1 \times 10^{-9} \text{ J/K}$ and $G = 1 \times 10^{-7} \text{ W/K}$, the thermal time constant is then $\tau = 10 \text{ ms}$ [36]. The peak power of the QCL used in previous experiments [15]-[18] is about 2.5 mW when operated at a pulse repetition frequency of 300 kHz. The effective power was degraded by the use of a Tsurupica window and a

Tsurupica lens in the beam each with approximately 64% transparency at 2.8 THz. For the time being, we will only consider one attenuating element, keeping in mind that this preliminary discussion represents the absolute upper performance limit for our system. Under these conditions the pixel temperature change in a 19200 pixel FPA is calculated to be about

$$\Delta T = 44 \mu\text{K}. \quad (0.9)$$

It should be noted at this point that this is a liberal estimate, since the 20% operational duty cycle of the QCL was not factored in, and the power incident on and absorbed by the FPA was assumed to be 100% of the incident flux which is not the case. To gain an appreciation for how the cameras should nominally respond to such signals, they must be compared to the figure-of-merit noise equivalent power (NEP). The derivation of NEP is made in the following sections, but the result for the IR-160 camera is 230 pW. The associated temperature change per pixel necessary to produce an image pixel with unit signal-to-noise ratio is then NEP/G, which is $\Delta T = 2.3 \text{ mK}$. That implies that it is impossible to detect individual laser pulses at 300 kHz using a microbolometer pixel with a ΔT of only $44 \mu\text{K}$. However, due to the relatively long time response τ compared to the laser's pulse period, we clearly detect measurable signals from the laser due to a cumulative effect from multiple pulses. Therefore the analysis needs to include not only the high frequency modulation component of the laser power, but also the quasi-static contribution coming from the effective averaging produced by the detector's slow response.

2. Analysis of Microbolometer Operation under Pulsed Power

When equation 1.8 was derived it was assumed that the average power is small, which is obviously not correct in reality. It is simply a consequence of linear small-signal analysis, commonly used in all formal derivations requiring only the frequency response. A more complete representation of Figure 11 includes the quasi-static power, expressed as P_0 , and the time varying power, $P_0 e^{j\omega t}$. The heat balance equation 1.4 can now be expressed as

$$P_0 + P_0 e^{j\omega t} = G\Delta T + C \frac{d\Delta T}{dt}. \quad (0.10)$$

This differential equation can be solved separately for each of the power terms (quasi-static and time varying) on the left hand side. Since we have already solved the modulated power term we will solve the unmodulated average power case, add the modulated solution and apply the boundary conditions. It follows that

$$\int \frac{d\Delta T}{\Delta T - P_0/G} = \int -\frac{1}{\tau} dt \quad \text{and} \quad \ln(\Delta T - P_0/G) = -t/\tau + \text{const.} \quad \text{Solving for } \Delta T \text{ we are left}$$

with the following.

$$\Delta T = \frac{P_0}{G} + \beta e^{-\frac{t}{\tau}} \quad (0.11)$$

Again, not all power incident on the device will be thermally absorbed depending on the absorptive properties of the material in a particular frequency regime and an efficiency factor η must be applied. Adding this to the previously solved modulated radiation yields the amount of the temperature change in a pixel as,

$$\Delta T = \frac{\eta P_0}{G} + \beta e^{-\frac{t}{\tau}} + \frac{\eta P_0}{G\sqrt{1+\omega^2\tau^2}} \sin(\omega t - \phi). \quad (0.12)$$

Applying the boundary condition $\Delta T = 0$ at $t = 0$ we find $\beta = \frac{\eta P_0 \sin(\phi)}{G\sqrt{1+\omega^2\tau^2}} - \frac{\eta P_0}{G}$. The

expression for the temperature change in a pixel is,

$$\Delta T = \frac{\eta P_0}{G} \left(1 - e^{-\frac{t}{\tau}} \right) + \frac{\eta P_0}{G\sqrt{1+\omega^2\tau^2}} \left(\sin(\omega t - \phi) + e^{-\frac{t}{\tau}} \sin \phi \right). \quad (0.13)$$

As time goes to infinity we are left with the final form of equation 1.14.

$$\Delta T = \frac{\eta P_0}{G} + \frac{\eta P_0}{G\sqrt{1+\omega^2\tau^2}} \sin(\omega t - \phi). \quad (0.14)$$

The second term in equation 1.14 is negligibly small at typical pulsing frequencies of the QCL, and the microbolometer response is essentially coming from the quasi-static term due to average power of the laser. The second term response (solid line) can be seen in Figure 12 for $P_0 = 1.25$ mW, $\eta = 0.64$, $G = 10^7$ W/K and $\tau = 10$ ms in a 19200 pixel array. Comparing this response to that of the first, average power term (dashed line) and

it is evident that beyond a pulse repetition frequency of 1 kHz the average power term dominates as the time varying term approaches 0.

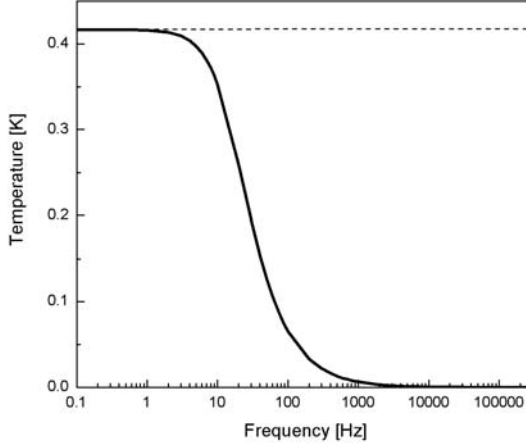


Figure 12. Temperature change in a pixel for $P_0 = 1.25$ mW, $\eta = 0.64$, $G = 10^{-7}$ W/K and $\tau = 10$ ms. Response of second term in Equation 1.14 (solid line) compared to average power term (dashed line) .

In order to gain an immediate understanding of the solution presented above we have used a technique to model the thermal and electrical properties of a microbolometer pixel in PSPICE [37]. The final form of the heat balance equation for the above solution is given as,

$$\eta P_0 + \eta P_0 e^{j\omega t} = G\Delta T + C \frac{d\Delta T}{dt}. \quad (0.15)$$

Using a simple RC circuit given in Figure 13 (a), the thermal parameter G (W/K) equivalent is the inverse resistance, R ($1/\Omega$), and the thermal parameter C (J/K) equivalent in the circuit is the capacitance, C_c (F). The power equivalent is the AC current $I(t)$ (A), and the temperature is therefore taken as the voltage response $V(t)$ (V). The heat balance equation is now presented in terms of electrical equivalents as

$$I(t) + I(t)e^{j\omega t} = \frac{1}{R}\Delta V(t) + C_c \frac{dV(t)}{dt}. \quad (0.16)$$

The thermal time constant $\tau = C/G$ is now represented as an RC time constant $\tau = RC_c$. Using the thermal parameters $C = 1 \times 10^{-9}$ J/K, $G = 1 \times 10^{-7}$ W/K and the thermal time constant $\tau = 10$ ms [36] we calculate the electrical equivalents as $R = 10$ M Ω , $C_c = 1$ nF and $\tau = 10$ ms. The peak power of the QCL used in previous experiments [15]-[18] is

about 2.5 mW when operated at 300 kHz. As calculated earlier, the associated temperature change per pixel in a 19200 pixel array was $\Delta T = 0.42$ K. This value was taken as the applied voltage in the circuit, with the equivalent voltage offset. Next the circuit behavior was modeled using analog modeling in PSPICE. Figure 13. (b) shows the temperature rise and decay, respectively, when the laser is on and off at a modulation frequency of 300 Hz for several time constants of a microbolometer pixel. At this frequency the time varying term is evident in the pixel response. Figure 13 (c) depicts the circuit response at 300 kHz. At such a high frequency, the rapid modulation response dies out, leaving only the quasi-static response. It shows, that for standard video rate, at 30 frames per second, THz imaging can be done using pulsed QCLs and micobolometers, provided that the average power of the laser is appreciable.

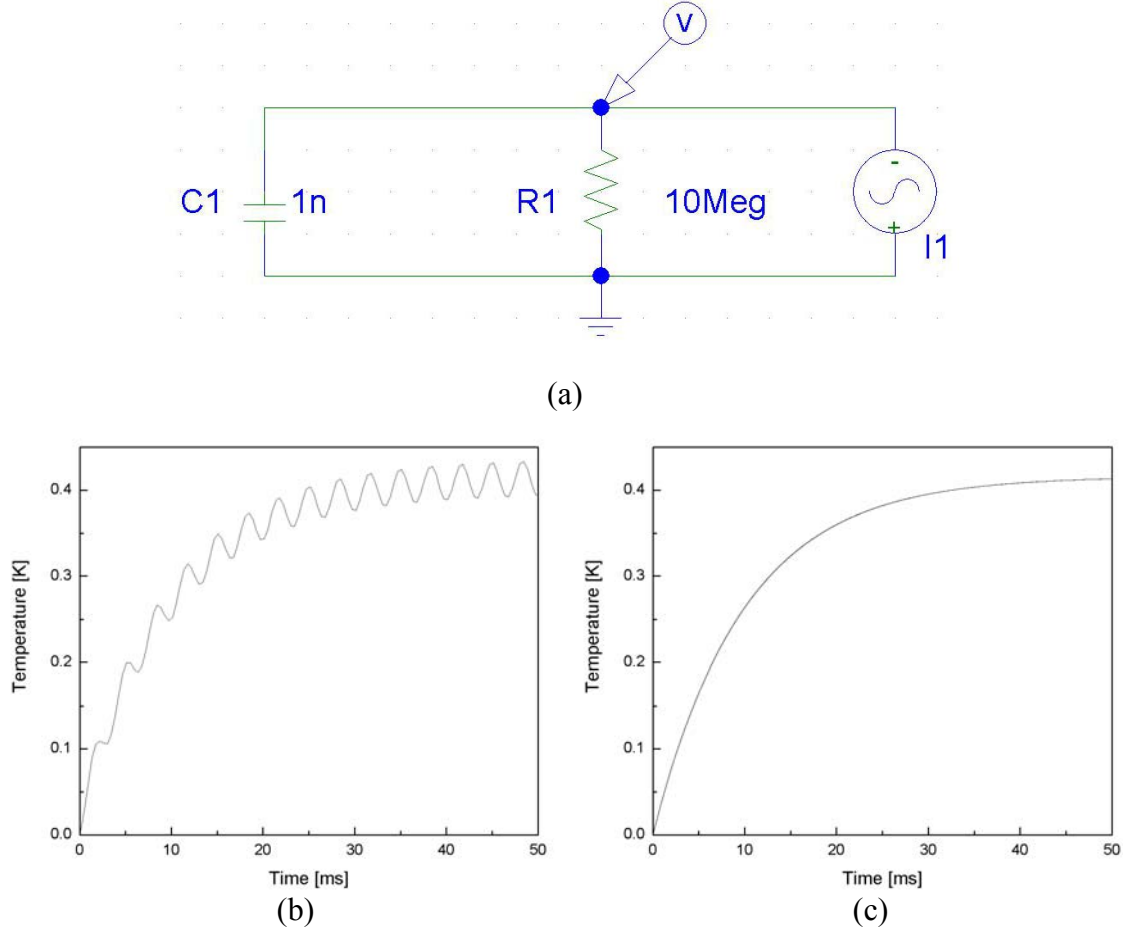


Figure 13. (a) RC circuit used to model equation 1.16. (b) 300 Hz PRF and (b) 300 kHz PRF.

3. Responsivity \mathcal{R}

The responsivity \mathcal{R} , is defined as the ratio of a sensors output signal to the input stimulus, which in this case is incident power. In the case of microbolometers, the change in resistance due to the temperature change is given by $\Delta R = \alpha R \Delta T$. Substituting for ΔT using equation 1.13, the change in resistance can be obtained as

$$\Delta R = \frac{\alpha R \eta P_0}{G} \left(1 - e^{-\frac{t}{\tau}} \right) + \frac{\alpha R \eta P_0}{G \sqrt{1 + \omega^2 \tau^2}} \left(\sin(\omega t - \phi) + e^{-\frac{t}{\tau}} \sin \phi \right). \quad (0.17)$$

The resistance change can be measured in a conventional Wheatstone bridge, as in Reference [36]-[37] using one microbolometer and three equal resistors. The current i through the side of the bridge with the device under an applied bias V_B is $i = \frac{V_B}{R_0(1 + \alpha \Delta T) + R_0}$ and $R_0(1 + \alpha \Delta T)$ is the resistance through the device. Solving for output signal of the bridge, V_{out} , gives the following expression,

$$V_{out} = \frac{V_B}{2} - \frac{R_0 V_B}{R_0(1 + \alpha \Delta T) + R_0}. \quad (0.18)$$

Assuming $\alpha \Delta T \ll 1$, then $\Delta V_{out} = (\alpha V_B \Delta T) / 4$. Using this result, the responsivity is found by dividing V_{out} by the incident power, P_0 , yielding

$$\mathcal{R} = \frac{\alpha V_B \eta}{4G} \left(1 - e^{-\frac{t}{\tau}} \right) + \frac{\alpha V_B \eta}{4G \sqrt{1 + \omega^2 \tau^2}} \left(\sin(\omega t - \phi) + e^{-\frac{t}{\tau}} \sin \phi \right). \quad (0.19)$$

Using $V_B = 5$ V, $\alpha = 0.02$ K⁻¹, $\eta = 0.64$, and $G = 1 \times 10^{-7}$ V/W and all other parameters unchanged gives

$$\mathcal{R} = 1.6 \times 10^5 \text{ V/W}. \quad (0.20)$$

A value of $\mathcal{R} = 2.0 \times 10^5$ V/W was previously reported in Reference [17] for the 8 to 12 μm spectral region, using only the frequency response term for a similar camera. These responsivities would allow us to see an image using the average power of the laser. If an entire focal plane were uniformly illuminated with a 1.25 mW average power beam, and the FPA consisted of 19200 pixels, the fraction of the power incident on a single pixel

would be about 65 nW, ignoring losses between pixels. The resulting voltage output would be about 10 mV, which can be easily measured.

4. Noise Equivalent Temperature Difference (NETD)

The noise equivalent power (NEP) of a device is the hypothetical input radiation power P_0 that would be required to create a detected signal-to-noise ratio of 1. The noise in a resistive bolometer is dominated by Johnson noise if the readout bias is less than 100 μ A [37]. If this is not the case, other noise sources can be significant and may include thermal, Johnson, 1/f and amplifier noise. Previous work [16]-[18] calculated the NEP for the IR-160 microbolometer and used the result to develop a NETD, equation 1.21, for the THz spectral region. That earlier treatment assumed only Johnson noise and made non-applicable assumptions about the bolometer resistance. Because of this, and the fact that 1/f noise in amorphous silicon can vary by three orders of magnitude with growth technique [37], this method could not be applied to our Miricle camera. Instead, NEP was deduced for both cameras in the IR region and used to determine the NETD in the THz region.

NETD is defined as the temperature change of the target that produces a FPA signal equal to the total noise [34]. The NETD can therefore be expressed as

$$\text{NETD} = \frac{4F^2}{\tau_0 A (dP/dT)_{\lambda_1-\lambda_2}} \bullet \text{NEP} \quad (0.21)$$

where F is the f-number of the lens, A is the pixel area, and τ_0 is the product of transmittance of the lens, absorptivity of the FPA, and the thermal emissivity of the target object. The differential spectral radiance dP/dT is the change in power per unit area radiated by a blackbody at temperature T , with respect to T , between some predetermined wavelength limits λ_1 and λ_2 . This differential is calculated from the spectral radiance, as given by Plank's Radiation Law, equation 1.22, and depicted in Figure 14.

$$P(T) = \frac{2\pi h}{c^2} \frac{v^3}{e^{hv/kT} - 1} \quad (0.22)$$

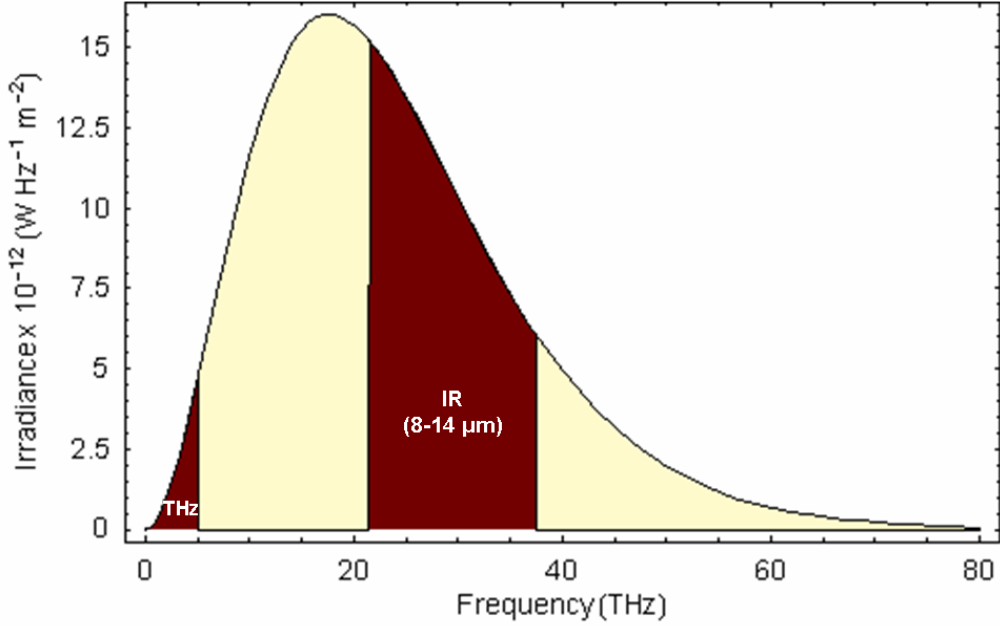


Figure 14. Spectral Radiance of a blackbody at 300K (from[16]).

Typical values for dP/dT in the 3-5 μm and 8-14 μm range for a 295 K blackbody are $2.10 \times 10^{-5} \text{ W cm}^{-2}\text{K}^{-1}$ and $2.62 \times 10^{-4} \text{ W cm}^{-2}\text{K}^{-1}$, respectively [34]. To determine this quantity in the terahertz range $P(T)$ can be found from

$$P(T) = \int_{v_1}^{v_2} \frac{2\pi h}{c^2} \frac{v^3}{e^{hv/kT} - 1} dv, \quad (0.23)$$

if it is assumed that the source is an ideal blackbody. Because we are at the low frequency limit of the blackbody spectrum, the Plank formula (1.23) may well be approximated by the Rayleigh-Jeans formula. Since $hv/kT \ll 1$ and $x = hv/kT$ is small, $e^x \sim 1+x$, and we are left with the following:

$$P(T) = \int_{v_1}^{v_2} \frac{2\pi h}{c^2} \frac{v^3}{1 + hv/kT - 1} dv, \quad (0.24)$$

$$P(T) = \int_{v_1}^{v_2} \frac{2\pi kT}{c^2} v^2 dv. \quad (0.25)$$

To a good approximation, the lower limit of integration can be set to 0. Setting the upper cut-off frequency to be v_c , the integral in equation 1.25 is then reduced to

$$P(T) \approx \frac{2\pi k T}{3c^2} v_c^3. \quad (0.26)$$

The quantity dP/dT is given simply as

$$\frac{dP}{dT} = \frac{2\pi k}{3c^2} v_c^3. \quad (0.27)$$

This value is found to be $4 \times 10^{-6} \text{ W cm}^{-2} \text{ K}^{-1}$, using $v_c = 5 \text{ THz}$. Substituting the result into equation 1.21 then gives the following expression for NETD at typical THz frequencies [16]-[18] :

$$\text{NETD} = \frac{6c^2 F^2}{\tau_0 A \pi k v_c^3} \bullet \text{NEP}. \quad (0.28)$$

Previous analysis of the IR-160 camera [16]-[18] yielded an NETD of 3 K with a cut off-frequency of 5 THz. This contrasts significantly with the NETD of 0.1 K that is typical in the IR spectral region. The increase in NEDT indicated the need for additional illumination for imaging in the THz frequency range.

As mentioned earlier, the NETD of 3 K in the THz region was based on NEP calculations made with approximations. Since the NETD is known for both cameras in the IR spectral region along with dP/dT of $2.62 \times 10^{-4} \text{ W cm}^{-2} \text{ K}^{-1}$ [34] in that region, we can make a direct calculation of the NEP which remains constant in all regions. The NETD of the IR-160 camera is $< 100 \text{ mK}$ with a f/0.8 germanium lens and $50 \times 50 \mu\text{m}^2$ pixel. The target emissivity is taken as 1, the germanium lens with anti reflective coating has a transmittance of 90%, and the SiN mean absorptivity is 80% [38]. Because of the fact that the camera was engineered for almost complete IR absorption in the $7 - 14 \mu\text{m}$ range, we will take its absorptivity as 1, but this will not necessarily be the case for the THz regime. Using these values in equation 1.22 gives a NEP in the 7 to $14 \mu\text{m}$ region of 230 pW for the IR-160 camera. The Miricle camera has a $35 \times 35 \mu\text{m}$ pixel, a NETD of $< 50 \text{ mK}$ and a, f/1 germanium lens with anti reflective coating. Its NEP is calculated to be 36 pW.

Using these values an accurate NETD for the THz spectral region can be extrapolated. The Tsurupica lens used for THz imaging is a f/1 untreated lens with a mean transmission of 0.60 in 1 to 5 THz range. Because the microbolometers used were

not designed for operation in the THz region the absorptive properties of the FPA cannot be assumed to be unity. The mean absorptivity in the THz region for SiN (used in the IR-160) is 40% and for Si (used in the Miricle 110K) is 10%. These values, along with a dP/dT of $4 \times 10^{-6} \text{ Wcm}^{-2} \text{ K}^{-1}$ reported earlier, give NETDs of 38 K for the IR-160 camera and 49 K for the Miricle camera. This predicts that the Miricle camera should be better at imaging in the IR spectral region with diminished performance in the THz regime compared to the IR-160 camera. In the next section, terahertz propagation through the atmosphere and different military relevant materials are presented.

C. THZ TRANSMISSION IN THE ATMOSPHERE AND MATERIALS

Losses in uniformly absorbing material can be characterized by Beer's Law

$$P = P_o e^{-\alpha x}, \quad (0.29)$$

where α is the absorption coefficient per unit length x of propagation through a material. At THz frequencies the effect can vary significantly between materials and frequency across different intervals. In a THz imaging system, careful operating frequency selection is critical for standoff imaging. A delicate balance must be struck between undesirable attenuation, from optical components and the intervening atmosphere, and desirable attenuation created by the target material. Each of these components will be addressed separately.

1. Atmospheric Transmission

Probably the most discouraging effect that limits the feasibility of stand-off THz imaging is the atmosphere, where water vapor is the dominant absorber that attenuates THz power drastically [39]. Several computer codes like LOWTRAN, MODTRAN and HITRAN have been developed to quantify atmospheric effects [40]. For propagation modeling of narrow bandwidth radiation, high resolution is required and for this FASCODE has been developed. FASCODE accesses the HITRAN database directly and many of the models in LOWTRAN indirectly like, molecular continuum absorption, molecular scattering, and aerosol absorption and scattering but at a much higher resolution [40]. Figure 15. was generated from FASCODE with a resolution of 100

MHz at an altitude of 100 m on a clear day with 50 km visibility. The path was a 1 m horizontal column at sea level and the frequency band was between 1.5 and 5 THz.

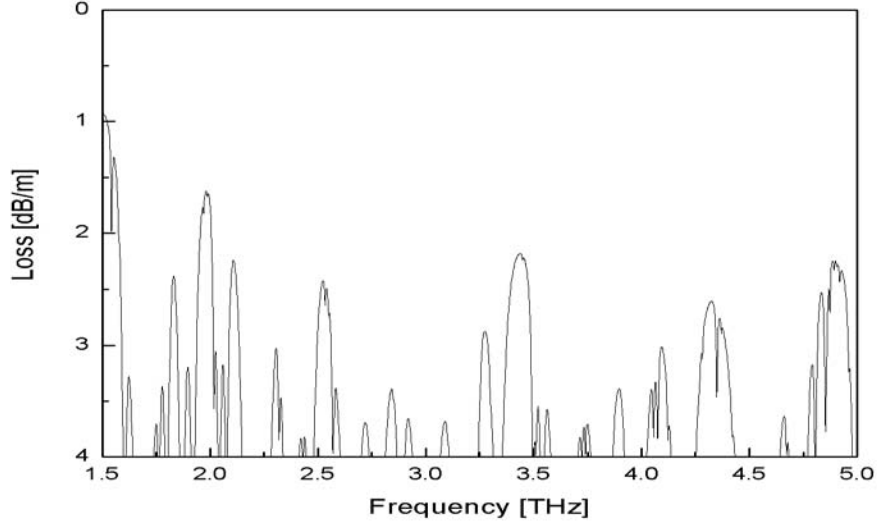


Figure 15. FASCODE model of atmospheric loss at sea level on a clear day.

For imaging done in this thesis two lasers of 2.8 and 3.6 THz were used. Originally being considered was a demonstration of stand-off imaging, but Figure 16. shows why this was not feasible due to strong atmospheric absorption at these frequencies. Imaging distances had to be carefully limited in all experimentation.

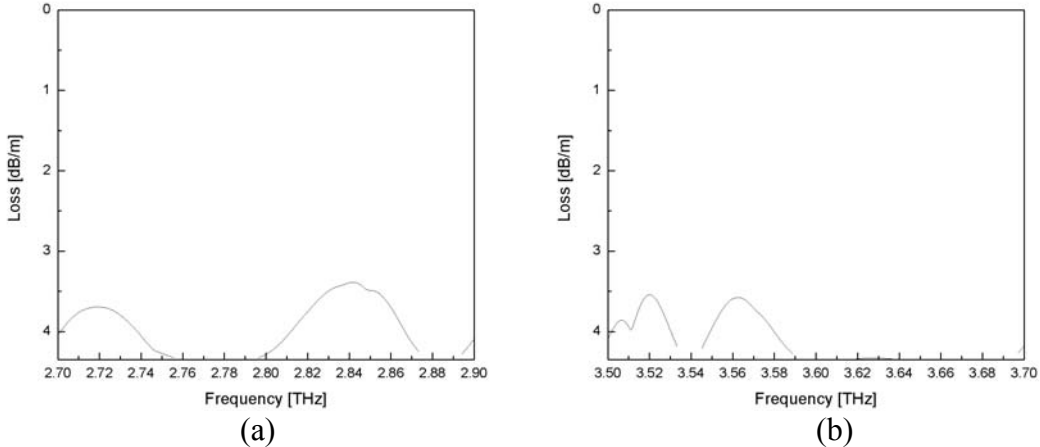


Figure 16. FASCODE model of atmospheric loss for a) 2.8 and b) 3.6 THz windows.

The FASCODE model in the THz region may not be entirely correct. The HITRAN model by itself gives fairly accurate predictions compared to FTIR analysis of the atmosphere as shown in Reference [14]. In Figure 17 (a) we can see that the losses

predicted by HITRAN at 296 K and 40% relative humidity are significantly less than those predicted in Figure 15 using FASCODE. The regions expanded in (b) and (c) show the results of FTIR analysis (dashed line) under the same conditions compared to the HITRAN model (solid line). Figure 18 (a) and (b) are provided as a comparison to the FASCODE model.

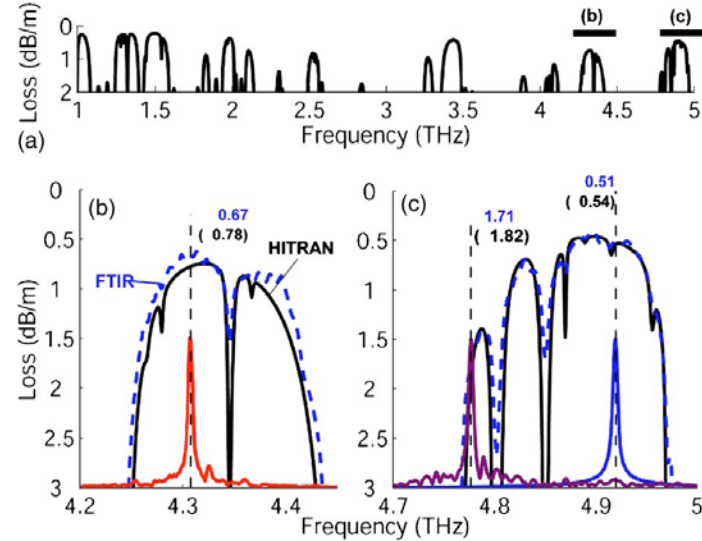


Figure 17. a) HITRAN model and FTIR results of atmospheric loss for b) 4.3 and c) 4.9 THz windows. HITRAN (solid line) and FTIR results (dashed line). Lasing spectra of QCL's are depicted with dashed vertical lines (from [14]).

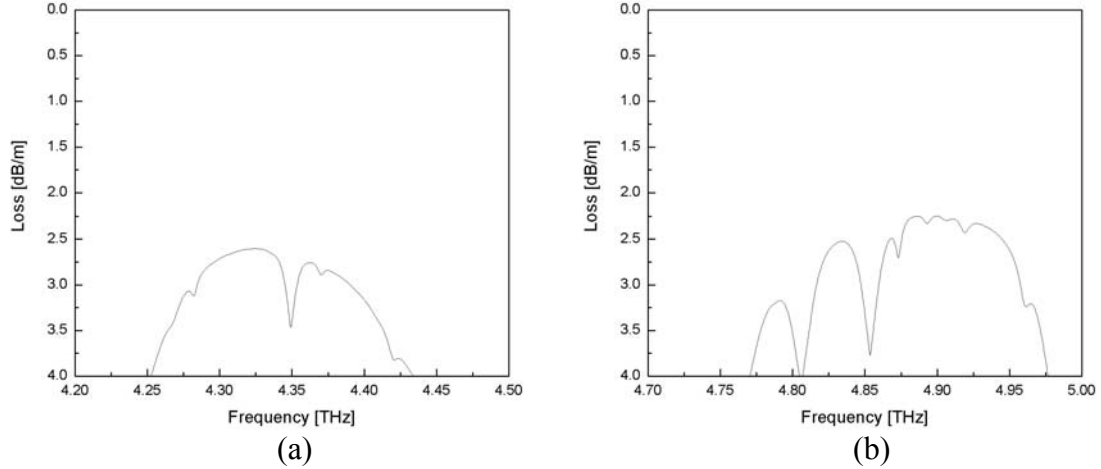


Figure 18. FASCODE model of atmospheric loss for a) 4.3 and b) 4.9 THz windows.

2. THz Laser Beam Propagation

To gain an appreciation of the feasibility of stand-off detection using a QCL/microbolometer imaging combination, the propagation of the laser beam through the atmosphere has to be considered in conjunction with the responsivity of the camera. Later we will see that a 1.25 mW average power beam is sufficient to image through an 18% transmissive target material and two 64% transmissive optical components. The images produced were at the lower limit of our experimental sensitivity, so it can be said that the lowest power incident on the FPA to allow imaging with the IR-160 camera is 92 μ W. Before we consider beam size and intensity, we can use this lower limit of detectable power to determine the absolute upper range limits possible for stand off-imaging. Due to the extreme atmospheric attenuation at the operating frequencies of our current QCLs, propagation distances will be estimated for the next laser to be used by the SRL, a 200 mW, 4.9 THz QCL. Using equation 1.29, the attenuation is calculated over distance for the FASCODE model, HITRAN model, and measured FTIR extinction coefficients shown in Figure 19.

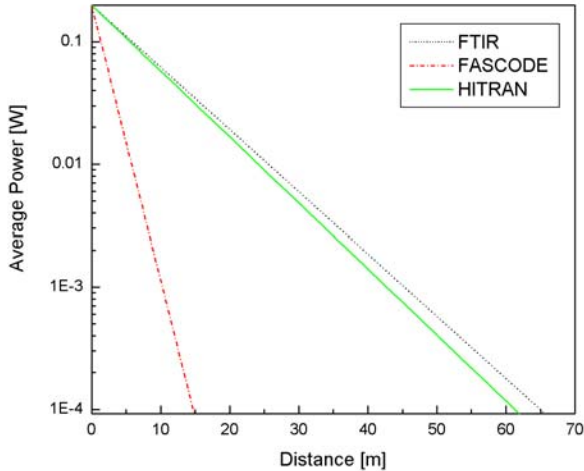


Figure 19. Maximum propagation distance for 200 mW 4.9 THz QCL using FTIR measured, FASCODE modeled and HITRAN modeled extinction coefficients.

When the beam divergence and losses due to optics are considered, the distances shown in Figure 19 to permit detection of a 92 μ W beam at the FPA will, of course, be reduced. Because of the structure of QCLs (see Figure 7 (b)) and their long operating wavelengths relative to the sizes of optical components, the beam emitted can be

divergent due to diffraction. It is necessary to collect and then to collimate the beam with parabolic mirrors to obtain an approximately collimated beam capable of travelling any significant distance.

3. FPAs, Optical Components (Tsurupica) and Plastic Tape

The next most critical component in our THz imaging system was the microbolometer FPA. Early in the experimentation process it was believed that the lower NETD of the Miricle camera in the infrared range would yield better results, but it was quickly apparent that poor absorption efficiency of THz radiation by the FPA pixels generated inferior images. Figure 20 (a) and (b) show the transmittance of THz through SiN (used in IR-160 camera) and amorphous Si (used in Miricle camera), respectively. It can also be noted that the transmittance differs markedly with frequency. The IR-160 FPA is a VO_x film on SiN, and it is evident in Figure 20 that at both 2.8 and 3.6 THz this material is drastically more absorptive than the amorphous Si used in the Miricle 110K camera. Interestingly, the figure also explains the improved imaging attained by the IR-160 camera at 3.6 THz from that of 2.8 THz in previous work done by the SRL [16]-[18].

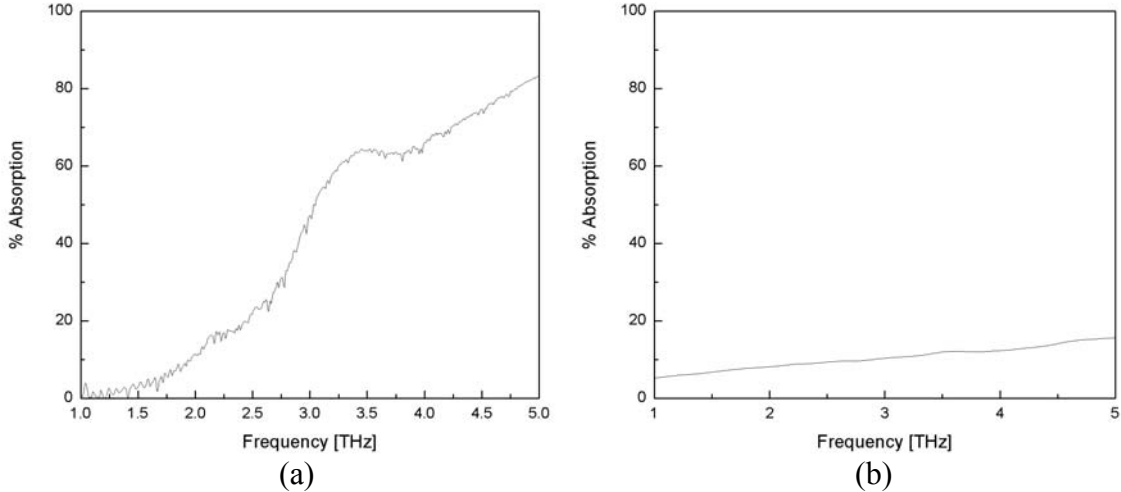


Figure 20. Percent absorption of FPAs. (a) SiN and (b) Si (after [41]).

The next materials analyzed were the Tsurupica used for the cryostat windows and camera lenses and the plastic tape used to obscure the knife blade in previous experiments [16]-[18]. The Tsurupica absorption was important to quantify since there were two components in the imaging system, the window and lens made of this material.

Materials were analyzed using a Nicolet Magna 850 Fourier Transform Infrared (FTIR) spectrometer. The spectrometer generates FIR radiation from an Ever-Glo blackbody light source in the 700 to 50 cm^{-1} wavenumber range. The internal beam splitter was a solid substrate, and the detector was a deuterated triglycine sulfate (DTGS) pyroelectric detector. Samples were introduced into the internal sample holder and scanned at a mirror velocity of 0.6329 cm/s for a total of 32 background scans and 32 scans of the sample. The resolution of the scans was 4 cm^{-1} . It was not experimentally viable to scan the focal plane material of the two cameras, SiN and amorphous Si elements. Data previously obtained from a similar FTIR spectrometer was accessed from the RIKEN THz database [41].

Figure 21 (a) and (b) show measured transmittances using our FTIR for Tsurupica and Polytape, respectively, in the 1.5 to 6 THz range. Only about 60-64% of the beam power (P_o) passes through these components at 2.8 and 3.6 THz frequencies. For this reason, optical components like lenses had to be used sparingly, and highly THz-reflective gold plated paraboloidal mirrors had to be used to steer and to manipulate the THz beam. Also seen in Figure 21 (b) is the highly THz-transparent quality of the tape used to conceal the knife blade in previous measurements [16]-[18]. A significant amount of success was achieved imaging metallic objects through this material.

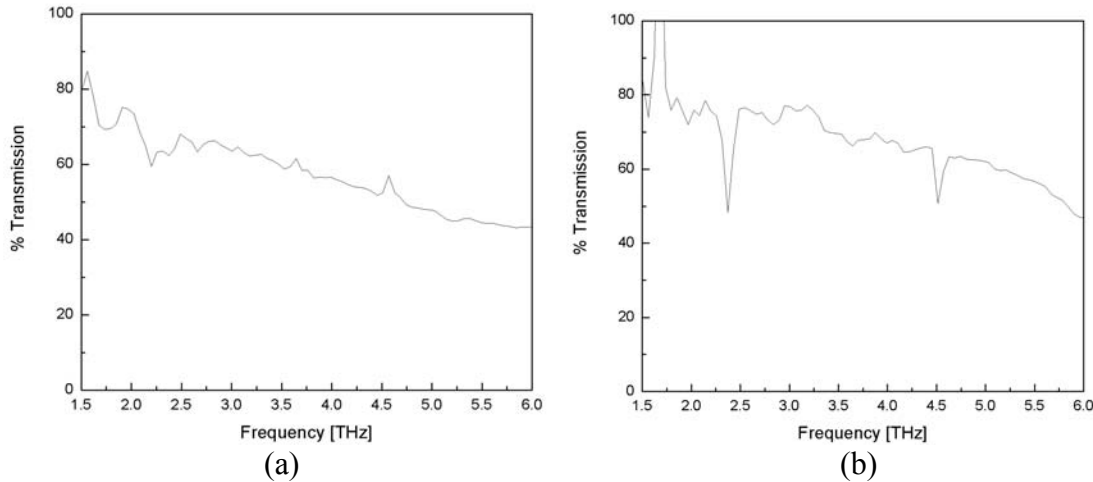


Figure 21. Percent transmission of (a) Tsurupica 4.0 mm, and (b) polytape 0.25 mm.

To further advance this work new and more challenging materials were sought. Of particular interest was a class of materials designed to conceal military assets that were specifically designed to defeat detection systems operating in other areas of the EM spectrum. These materials are discussed below.

4. Camouflage and Suppression of Military Assets

Some commonly used methods for concealing military assets are screens, blankets, heat reduction systems, and mobile camouflage nets. There is a significant amount of theory behind the operation of all these measures [42] that are designed to suppress detection across most areas of the electromagnetic spectrum, from UV to radar. Due largely to a lack of sources and detectors, the THz spectrum has not yet been exploited, nor have adequate countermeasures been developed. Some properties of THz radiation, like its ability to penetrate materials, make it difficult to counter with the systems mentioned above. When considered in conjunction with the inherently high reflectivity of metals and ceramics at THz frequencies, this leads to tantalizing possibilities for real-time imaging of concealed military assets from modest stand-off distances. A number of these systems were analyzed at THz frequencies in the results section, 5-B.

IV. EXPERIMENTAL SET UP AND THZ IMAGING

A. OPTIMIZATION OF QCL POWER

The first step taken towards studying improved THz imaging capability was enhancing the optical power emitted by the 2.8 and 3.6 THz QCLs. As mentioned earlier, previous analysis of laser performance concentrated on optimizing optical power by analyzing the duty cycle. The research reported in this thesis focused on optimizing the optical power by analyzing the dynamic impedance characteristics of the laser and matching impedances for the optimized operating frequency. The bracketing procedure outlined below yielded the optimal operating conditions for terahertz imaging.

The laser itself is housed in a Janis closed cycle refrigeration (CCR) system vacuum shroud. The atmosphere is removed from the CCR shroud using an Edwards Picodry pump. The cold finger within the shroud is cooled using a high pressure helium CCR system and is maintained at 10 K with a LakeShore 312 auto-tuning temperature controller. To dissipate the heat generated by the large currents pumped through the device, the QCL was mounted on a copper block heat sink attached to the cold finger of the refrigeration unit, as illustrated in Figure 22.

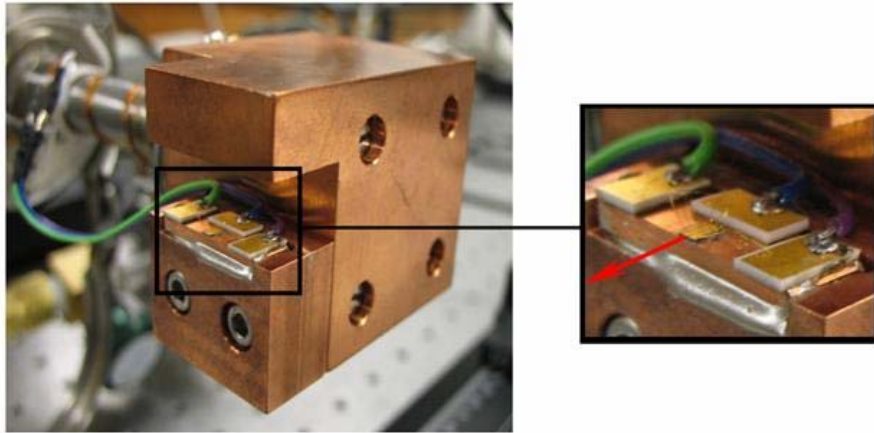


Figure 22. 3.6 THz QCL mounted on copper thermal dissipation block attached to cold finger. Red arrow in inset depicts direction of laser output beam. Shroud has been removed from the CCR system (from [16]).

The window of the shroud was a 4 mm thick Tsurupica plate whose THz transmission properties can be seen in Figure 21. The beam was collected and collimated by a 50.8 mm focal length gold plated off axis-parabolic (OAP) mirror, and steered with a gold plated flat mirror into the external port of the FTIR spectrometer. The QCL was driven with an Agilent 8114 100 V, 2 A pulse generator, equipped with a variable output impedance selection capability. The frequency was varied from 1 to 400 kHz, with impedances of 5Ω , 10Ω , 15Ω , and 20Ω . Impedances were further bracketed using a frequency that produced the most optical power as measured by the FTIR. Once the impedance matching of the signal generator to the load of the QCL was found, we then investigated whether the transformer used in previous experiments [16]-[18] provided a better impedance match and improved optical power output. This defined the impedance that would be used subsequently for improved imaging.

The pulse repetition frequency (PRF) was then refined using the aforementioned optimal impedance value. Optical power measurements were taken for 1, 100, 200, and 300 kHz PRF by varying the current from 0.5 A to 1.6 A for the 3.6 THz laser and 0.5 A to 1.4 A for the 2.8 THz laser. This identified the optimal PRF.

Next the duty cycle was investigated briefly. Previous imaging using this laser determined that a 20% duty cycle was optimal for short duration lasing. This conclusion needed to be confirmed for our new optimal operating parameters. Previous studies also concluded that operating time affected performance. The effect on optical power was analyzed over 1 min and 5 min times using the new impedance parameters and the various frequencies investigated before. These results were plotted to determine the best operating frequency for short term and sustained imaging applications.

The laser I-V characteristics were then taken for both the 2.8 and 3.6 THz lasers, based on their optimal settings found from the above procedure. The voltage and current were measured with an Agilent Infiniium Oscilloscope, and the optical output was measured concurrently from the FTIR spectrometer.

B. OPTIMIZED IMAGING ARRANGEMENT

Imaging was achieved using the optical set up previously established by the SRL [16]-[18]. The optical arrangement can be seen in Figure 1. This thesis research optimized the optical path to achieve improved imaging. The exact procedure is described below. Both QCLs were driven with an Agilent 8114 pulse generator at 300 kHz PRF and a 20% duty cycle. For the 2.8 THz QCL, a 1.3 A current was applied and impedance matched at $5\ \Omega$. The 3.6 THz QCL had an applied current of 1.4 A and was impedance matched at $13\ \Omega$. The QCLs were cooled to 10 K using the Janis CCR system described above. The shroud window was a 4 mm Tsurupica flat with transmission of 64% and 60% for the 2.8 and 3.6 THz QCLs, respectively. The devices were placed as close to the window as possible within the shroud, and the highly divergent THz beam was captured using a 50.8 mm focal length gold plated OAP mirror. This mirror was placed inverted and close to the device outside of the shroud so an un-collimated beam emerged. The beam was sent to a second OAP mirror of focal length 101.6 mm. The second mirror was placed approximately 160 mm above the first mounted on the same optical post. A Tsurupica 1/f lens with a focal point of 20 mm was then attached to the camera to focus the image on the FPA as illustrated in Figure 23. The use of an off-axis paraboloidal mirror to collect the output radiation from the QCL and then concentrate it on the sample was not an optically optimized way to proceed. The better choice would have been an ellipsoidal mirror, but one was not available.

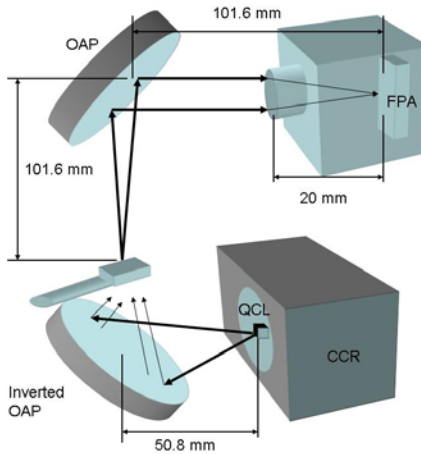


Figure 23. Schematics of the optics used in THz imaging.

THIS PAGE INTENTIONALLY LEFT BLANK

V. RESULTS

A. OPTIMIZATION OF QCL PERFORMANCE

The 3.6 THz QCL was driven by the pulse generator with 1.4 A, 10% duty cycle at frequencies from 1 to 400 kHz and impedances of 5, 10, 15, and 20 Ω . Figure 24 (a) shows that peak optical power production is achieved somewhere between 1 and 100 kHz PRF and around 15 Ω impedance. A frequency of 100 kHz was chosen to further bracket the impedance match that produced the most optical power as measured by the FTIR spectrometer. Figure 24 (b) shows this occurring at a 13 Ω impedance.

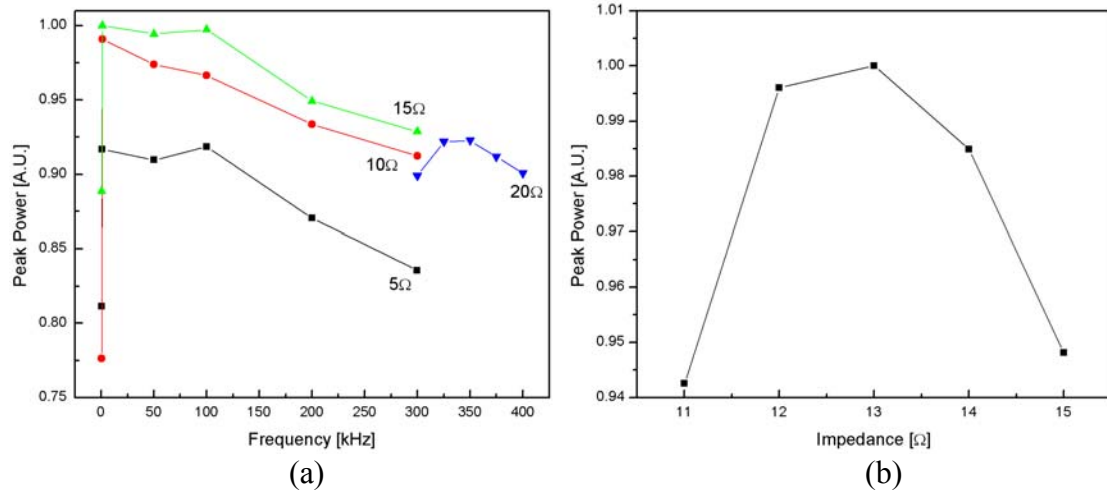


Figure 24. (a) Peak power of the device given a pulse generator impedance 50 Ω into 5, 10, 15 and 20 Ω at various frequencies, and (b) peak power of the device at 100 kHz given a pulse generator impedance of 50 Ω into 11 to 15 Ω .

Knowing the optimal impedance match for the device, we verified the performance by again looking at the optical output for 1, 100, 200, and 300 kHz PRF. This was done for both the optimal 13 Ω impedance and for the outlying impedances, since it is possible the device impedance may be frequency dependent. Figure 25 (a) confirmed that the optimal impedance match and frequency combination was 13 Ω and 100 kHz PRF. This also yielded the optimal current as 1.55 A. Since previous experiments used a frequency of 300 kHz and a transformer to impedance match the device and driver, the new results had to be compared to prior performance, given these

different parameters. Figure 25 (b) shows a drastic improvement at a current of 1.55 A, 100 KHz PRF and a 13Ω impedance. It also shows that previous experiments were achieving promising results with only 70% of the available optical power.

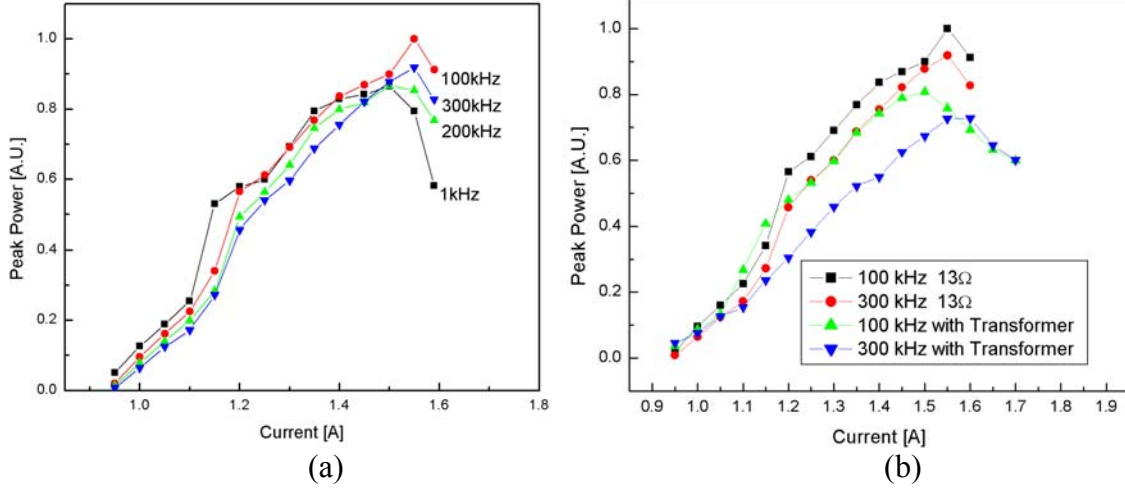


Figure 25. (a) Peak power of the device given a 10% duty cycle, and a pulse generator impedance of 50Ω into 13Ω for various currents and pulse frequencies, and (b) peak power of the device given a 10% duty cycle, and a pulse generator impedance of 50Ω into 13Ω or with transformer for various currents and PRF of 100 and 300 kHz.

The 20% duty cycle was assumed to be optimal from previous experiments [16], but the optimization above had to be done at 10% to avoid damaging the device. The power available at 20% the duty cycle was investigated briefly as shown in Figure 26 (a), where over a two-fold increase in optical power was obtained with operation at 20% vice a 10% duty cycle. Previous studies also concluded that there is an effect on performance with operating time. Figure 26 (b) shows the effect on optical power over time (1 min and 5 min) using a 13Ω impedance and the various frequencies investigated before. These results indicate the best operating frequency for short term and sustained imaging is again 100 kHz.

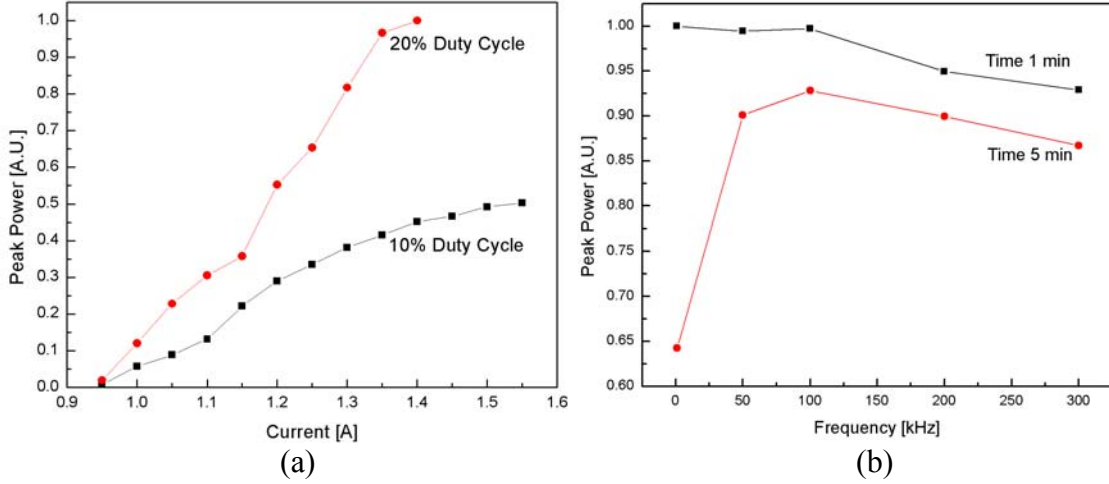


Figure 26. (a) Peak power of the device at 100 kHz for 10 and 20% duty cycles, with a pulse generator impedance of $50\ \Omega$ into $13\ \Omega$ at various currents, and (b) peak power of the device given a 10% duty cycle, with a pulse generator impedance of $50\ \Omega$ into $13\ \Omega$ at various frequencies after 1 and 5 minutes of lasing.

The above analysis was undertaken for the 2.8 THz laser, with minor modifications. Care had to be taken, and the device performance was not pushed as hard as possible, since at the conclusion of the analysis above the 3.6 THz laser ceased to operate and was no longer available for imaging experiments. Figure 27 shows the results of the iterative process that again yielded 100 kHz as the optimal operating PRF with a device impedance of $5\ \Omega$.

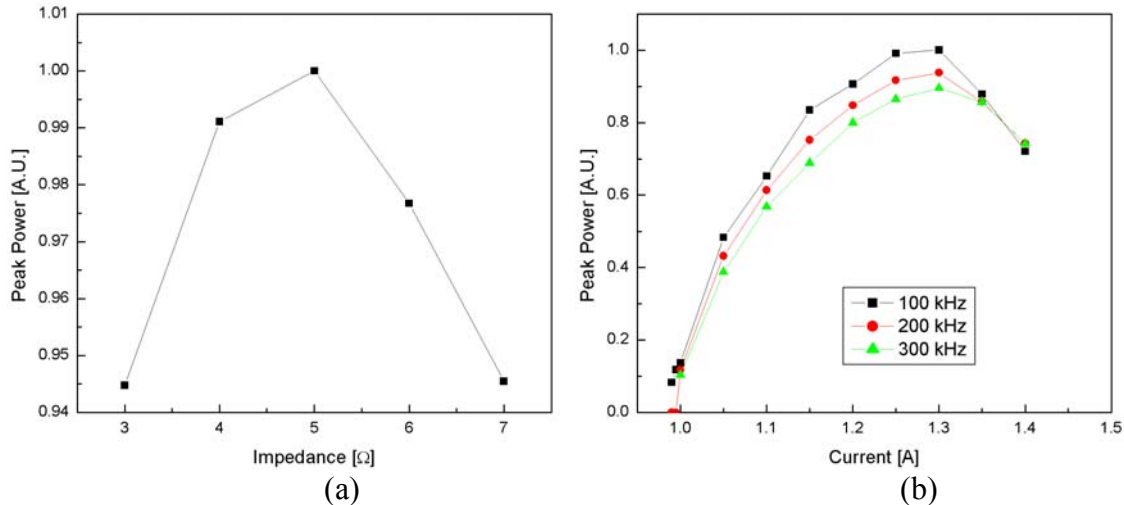


Figure 27. (a) 2.8 THz QCL peak power given a 10% duty cycle, and a pulse generator impedance of $50\ \Omega$ into 3 to $7\ \Omega$, and (b) peak power given a 10% duty cycle, and a pulse generator impedance of $50\ \Omega$ into $5\ \Omega$ for various currents and PRFs.

Finally the I-V characteristics of the two devices were investigated using the optimized parameters generated above. Figure 28 (a) and (b) show the I-V curves for the 3.6 and 2.8 THz lasers, the threshold current for lasing and the applied current and bias that resulted in optimal optical power output.

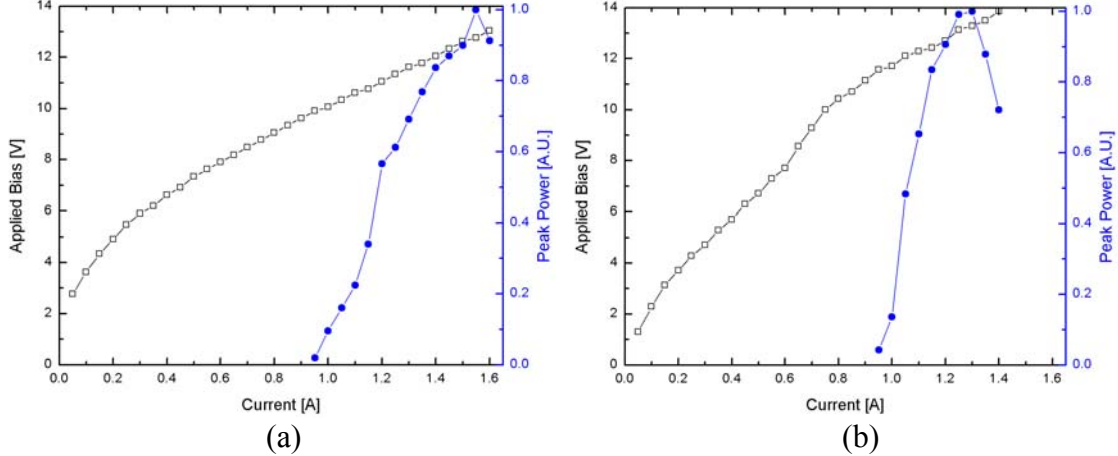


Figure 28. a) I-V characteristics and peak power output of the 3.6 THz QCL given a 10% duty cycle, with a pulse generator impedance of $50\ \Omega$ into $13\ \Omega$ at a PRF of 100 kHz, and b) I-V characteristics and peak power output of the 2.8 THz QCL given a 10% duty cycle, with a pulse generator impedance of $50\ \Omega$ into $5\ \Omega$ at a PRF of 100 kHz.

B. ANALYSIS OF CAMOUFLAGE MATERIALS

Combat clothing is the most prevalent material used to conceal personnel. The analyzed sample of combat uniform is comprised of two types, one for temperate woodland regions and the other for arid regions. Both samples are 0.32 mm thick and are pictured in Figure 29 (a). The transmission spectra in Figure 29 (b) shows little promise for THz screening of military personnel clothed in this material, due to poor THz transmission.

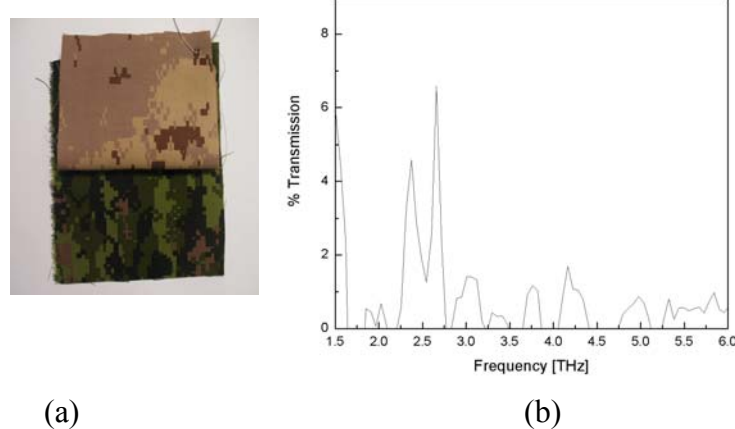


Figure 29. a) Photographs of combat uniform, arid region (top), 0.32 mm, and temperate woodland (bottom), 0.32 mm, and b) percent transmission of arid region combat uniform.

The next sample is a garnish for a temperate woodland camouflage screen. The garnish mimicking foliage consists of a green and black patches each 0.49 mm thick. The sample is pictured in Figure 30 (a). Since these materials typically do not conceal large metallic or ceramic objects, they likely could not be defeated by THz imaging system due to poor THz transmission.

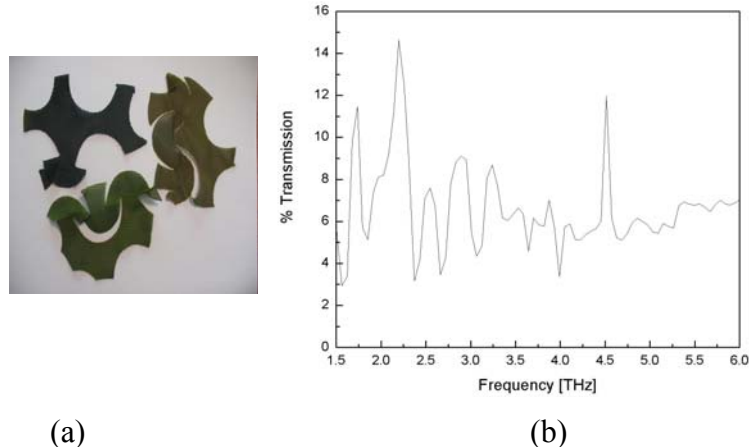


Figure 30. a) Photograph of temperate woodland camouflage screen, black and green garnish, 0.49 mm, and b) percent transmission of temperate woodland camouflage screen.

The next sample is from a blanket vice a garnish and is intended for winter operations. The sample is pictured in Figure 31 (a). As with the woodland screen, it holds little promise for THz imaging due to poor THz transmission (see Figure 31 (b)).

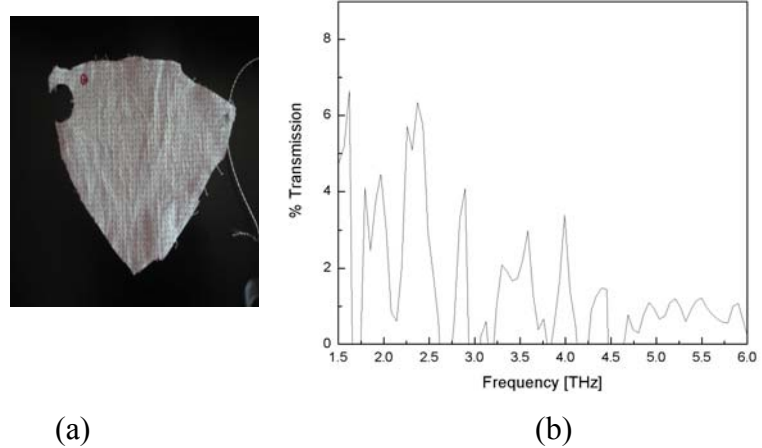


Figure 31. a) Photograph of winter operations camouflage screen, 1.12 mm, and b) percent transmission of winter operations camouflage screen.

Thermal blankets and heat reduction systems are commonly used to conceal metal and ceramic assets. The thermal blanket samples in Figure 32 (a) are for temperate woodland, arid regions and winter operations. THz transmission spectrum in Figure 32 is similar in all three samples and attenuates too drastically for practical imaging.

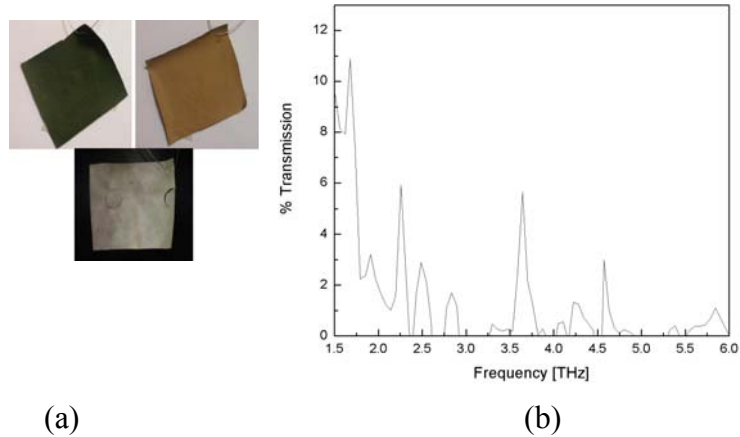


Figure 32. (a) Photographs of thermal blankets, temperate woodland (top left), arid (top right) and winter operations (bottom center), and (b) typical percent transmission for all samples.

The Heat Transfer Reduction System is comprised of an insulator, a 0.44 mm base fabric, and 0.16 mm scrim. The arid region system without the base layer is pictured in Figure 33 (a). Figure 33 (b) shows that the heat transfer reduction system

holds promise for imaging below 2 THz if it is used without the insulating layer. When used with the insulating layer THz energy is totally attenuated.

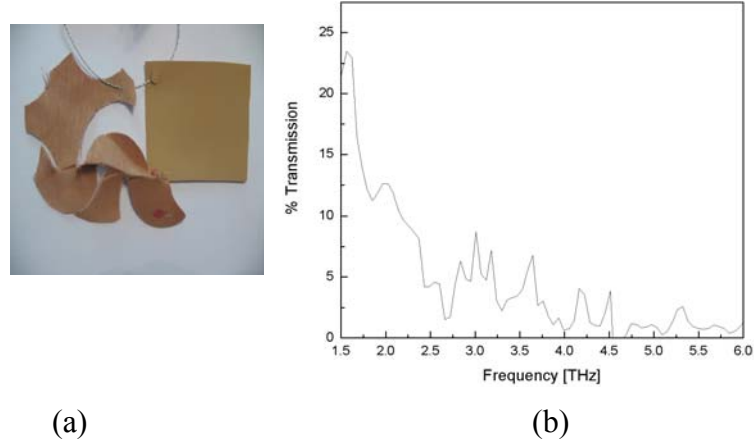


Figure 33. a) Photograph of heat transfer reduction system without insulating layer, base layer (right) and scrim (left), and b) percent transmission of heat transfer reduction system, base layer and scrim.

Camouflage nets are the most widely used means of concealing vehicles and other large assets. The analyzed sample is a garnish for temperate woodland camouflage netting used for vehicles. The garnish mimics foliage and consists of a green and black leaf pattern and a brown and black leaf pattern, each about 0.25 mm thick. The sample is pictured in Figure 34 (a). This material holds significant possibilities for THz imaging based on the transmittance spectra shown in Figure 34 (b). It possesses relatively good THz transmission properties and effectively conceals metallic and ceramic objects that reflect THz radiation strongly. The possibility of achieving reflective THz images from a system based on a UAV platform is very high. This material will be used for imaging studies in the experimental portion of the thesis.

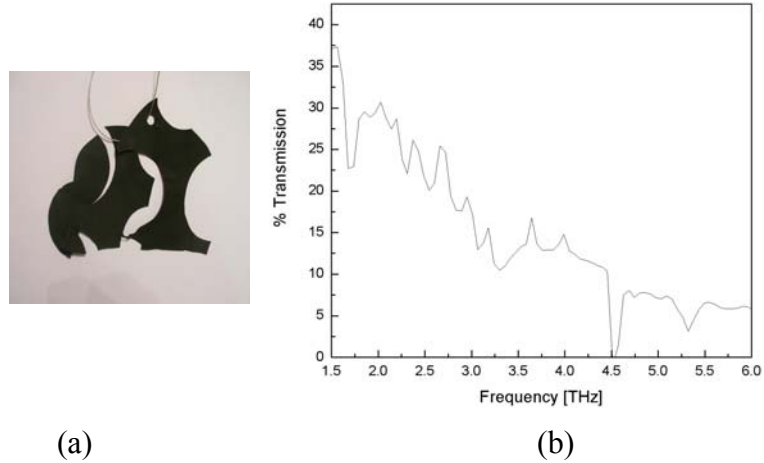


Figure 34. a) Photograph of woodland vehicle camouflage net, and b) percent transmission of garnish.

The next sample is a base layer and scrim for an arid camouflage system again used for vehicles. The material consists of a 0.50 mm base layer and 0.27 mm scrim. The sample is pictured in Figure 35 (a). Like the woodland vehicle camouflage net this material holds significant possibilities for THz imaging if the scrim is used alone. With the base layer employed it would defeat a THz imaging system.

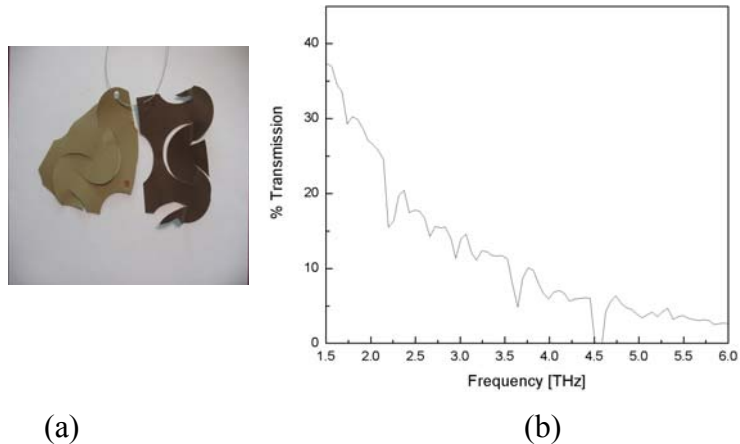


Figure 35. a) Photograph of the arid region mobile camouflage system, base layer (left) and scrim (right) and b) percent transmission of scrim only.

The last sample is a winter operations mobile camouflage system for vehicles. The system is comprised of a 3.43 mm backing, a 0.47 mm base layer and a 0.51 mm to 0.54 mm garnish layer. The system is pictured in Figure 36 (a). When elements are

employed either individually or together as a system they will defeat THz imaging systems, based on the transmission spectra shown in Figure 36 (b).

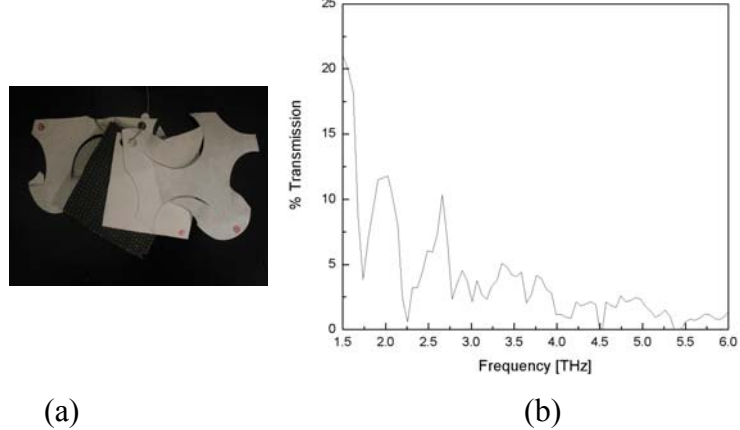


Figure 36. a) Picture of winter operations mobile camouflage system, garnish, backing layer, base layer, and garnish, and b) percent transmission base layer only.

C. PERFORMANCE OF TWO CAMERAS AND THZ IMAGING

Before performing any THz imaging, the respective performances of the two cameras were compared in the IR spectral region. Figure 37 (a) shows an optical image of the imaging setup used, along with the same view in the IR using the Miricle 110K (Figure 37 (b)) and IR-160 (Figure 37 (c)) cameras with their original optics. It can be clearly seen that the Miricle produces sharper image compared to the IR-160, due to its smaller pixel size and larger FPA format.

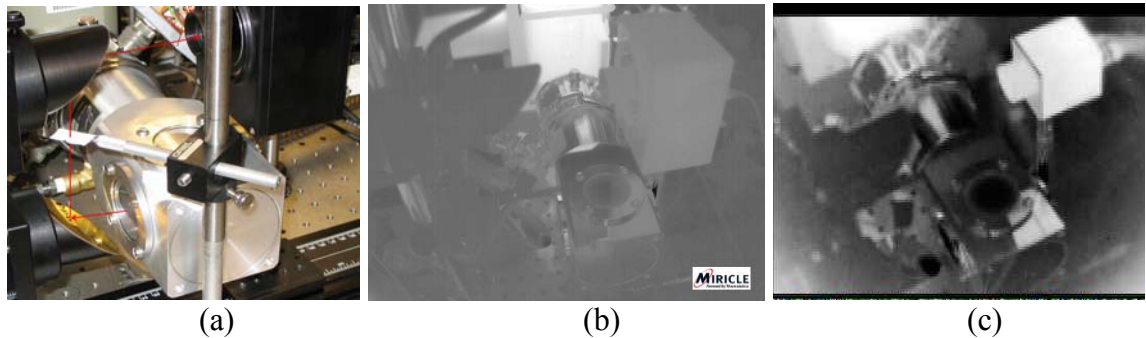


Figure 37. a) Photograph of the imaging setup (from [16]), b) IR image of (a) using Miricle 110K camera, and b) IR image of (a) using IR-160 camera.

Next, the two cameras were compared at THz frequencies using this optical setup and the 2.8 THz QCL. The beam was focused directly on the FPA using OAPs without the Tsurupica lens attached to the camera. A current of 1.3 A was applied to the QCL at 100 kHz PRF, 20% duty cycle and impedance matched at 5Ω . Figure 38 shows what was initially unexpected, the lower NETD camera (in the IR range) produced the weakest THz image. The THz absorptive properties of amorphous Si were compared to that of SiN (see Figure 20), and it was immediately obvious that we would have little or no success with the new camera due to weaker absorption efficiency of THz radiation by amorphous Si. Also apparent are the diffraction patterns above the beam which were the first indications that the imaging arrangement used in previous experiments [16]-[18] may not have had the optical properties originally thought.

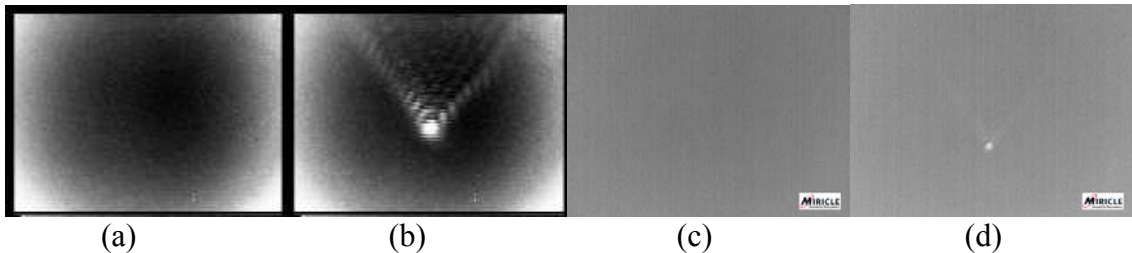


Figure 38. a) Background using Infrared Solution IR-160 camera, b) 2.8 THz beam using 50Ω into 5Ω at a PRF of 100 kHz, 20% Duty Cycle, c) background using Thermoteknik Miricle 110K camera and d) 2.7 THz beam using 50Ω into 5Ω at PRF 100 kHz.

The above findings brought the fact that FPA's behave very differently at THz frequencies than in the IR spectral region to the forefront of our investigations. As a second look at this important result, we looked at earlier published work done by the SRL.

The images created using 2.8 and 3.6 THz frequencies of the knife blade concealed in tape pictured in Figure 39 show a frequency dependence of image quality. The 2.8 THz image was slightly weaker than the 3.6 THz image taken with the IR-160 SiN based camera. From Figure 20, and assuming no reflection, the FPA should exhibit 85% absorption at 3.6 THz compared to 70% at 2.8 THz. Figure 20 (a) and (b) also show the absorption characteristics at 2.8 THz for Si at 40% and SiN at 70%. Clearly, the amorphous silicon based camera was not a good choice for THz imaging, as seen in

Figure 40. The 2.8 THz beam is seen with the Tsurupica lens in place in (a), and the unconcealed knife (b), and concealed knife (c), are just barely visible in the bottom left hand corner of the beam. As a consequence, no further imaging was attempted with the Miricle camera.

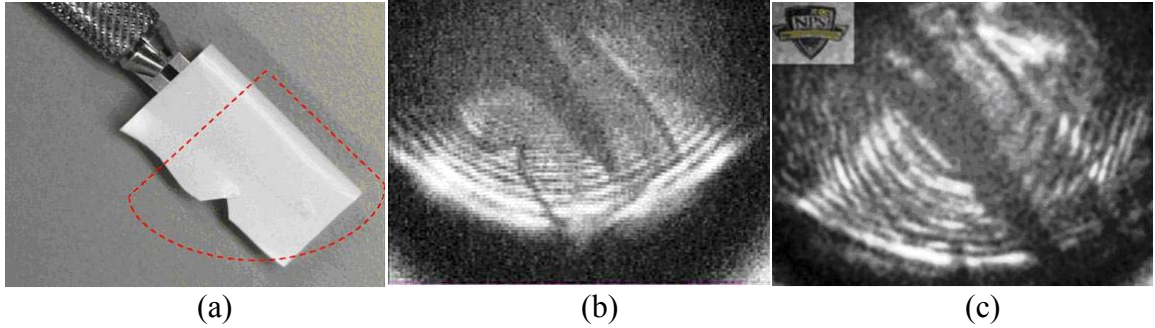


Figure 39. a) Knife concealed by plastic tape, b) 2.8 THz image using Infrared Solution IR-160 infrared microbolometer camera and c) 3.6 THz image using Infrared Solution IR-160 infrared microbolometer camera .

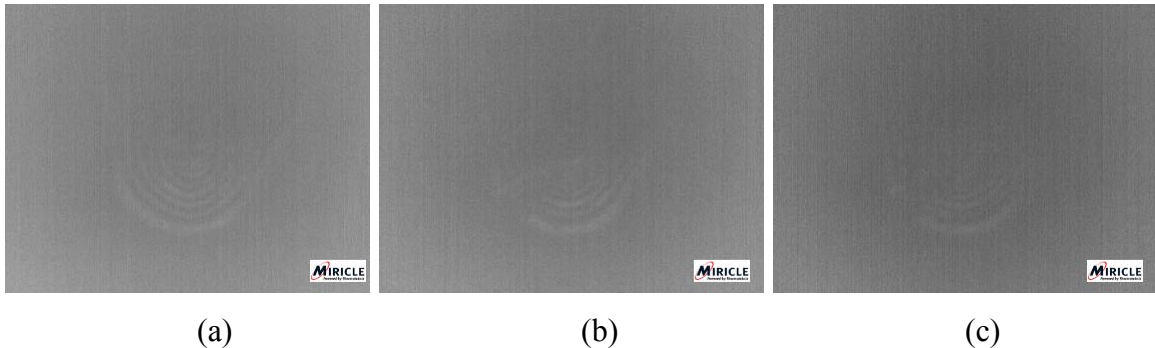


Figure 40. a) 2.8 THz beam, b) Un-obsured knife, and c) Knife obscured with tape.

Next, the identical imaging scenario was attempted with the IR-160 camera. Figure 41 (a) shows an identical beam pattern to that of the faint Miricle beam pattern above. The pattern is similar to that of previous imaging at 2.8 THz shown in Figure 40 (b). Interestingly, the results of optimizing the QCL can be seen in these images. Figure 41 (b) shows the un-obsured blade, and the hole in the blade can clearly be seen, where that was not the case previously. Figure 41 (c) shows the blade obscured by plastic tape where unlike the image in 39 (b) the only indication that the blade was obscured in the new image is a slight change in the diffraction pattern most noticeable in

the lowest ring. In fact, the presence of such a diffraction pattern implies that some fundamental assumptions about the optical setup may be questionable. This is discussed below, in the conclusions.

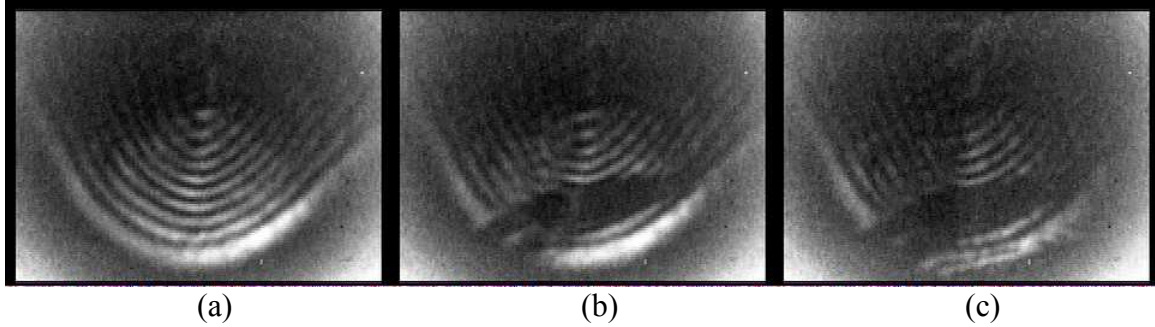


Figure 41. a) 2.8 THz beam, b) un-obscured knife and c) knife obscured with tape.

As a final experiment, the possibility of using this technology in a battlefield sensing environment was investigated. After analyzing numerous materials used for concealing military assets, the camouflage net was considered as possibly possessing THz vulnerabilities. At 2.8 THz the material was found to be 18% transmissive. The optical arrangement used to produce the above images was again used, and a small camouflage leaf was placed on the blade. Figure 42 shows how the knife is clearly visible under the leaf.

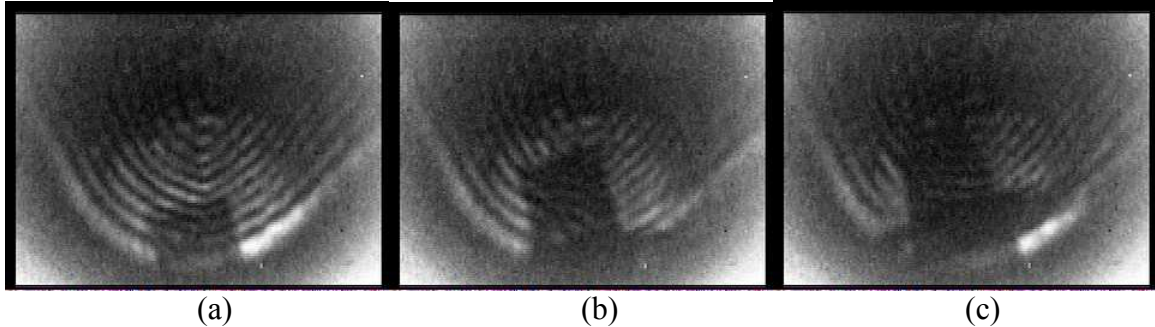


Figure 42. Knife covered with woodland camouflage net a) camouflage net coming into beam, b) covered knife coming into beam, c) covered knife fully visible in beam.

The significance of this image cannot be overstated. The ability to image through a material only 18% transmissive, at an average power of 1.25 mW, demonstrates the incredible potential of this technology. This proof-of-principle experiment clearly indicates the possibility of active THz imaging detection at a distance using an arrangement designed to operate in narrow atmospheric windows.

VI. CONCLUSIONS

The main aim of this thesis research has been to investigate how infrared optimized microbolometer absorbing membranes interact with THz frequencies and whether it will be feasible to perform active stand-off detection of concealed targets using THz radiation. In addition, a set of commonly used camouflage materials were also probed to determine their effectiveness and vulnerabilities in the THz spectral range.

During the course of research, it was found that in THz imaging using relatively slow microbolometer sensors and pulsed QCL sources, the most important parameter is the average power output of the source. The QCL is usually operated in pulsed mode with rate in the hundreds of kHz which is much higher than the cut-off frequency of microbolometers, which is typically of about tens of Hz. This indicated that neither camera should be able to detect the individual pulses of the THz beam. A detailed expression was derived to understand the response of microbolometer pixels to pulsed QCL sources, which clearly shows that the pixels can only respond to average power.

This directly influenced the need to reconsider QCL operation. Armed with this knowledge, a method was developed to optimize peak optical power by maximizing the average power that would be sensed by the microbolometer. The average power was optimal for both the 2.8 and 3.6 THz QCL's at 100 kHz PRF, and with impedances matched at $5\ \Omega$ and $13\ \Omega$, respectively.

A direct comparison of the optically modified IR-160 and Miricle 110K microbolometer cameras yielded surprising results. Earlier experiments were reproduced using the amorphous silicon based Miricle 110K camera to assess the image quality, but we found it to be inferior to the silicon nitride-based IR-160 camera. These observations indicated that the absorption of THz in amorphous silicon is much weaker than in silicon nitride. This was confirmed with an FTIR analysis of the two FPA materials. The differing camera response is predicted based on the absorption efficiency of the two materials.

In addition, for stand-off imaging applications, it is very important to select THz frequencies that propagate well through the atmosphere with minimal extinction. Correct frequency selection allows for operation in narrow atmospheric windows where attenuation is relatively low and a high average power fluency can be maintained between the camera and target. A frequency that minimizes attenuation through optical components and concealing materials, but interacts strongly with concealed objects must also be chosen correctly. Finally, based on this frequency selection, a focal plane array material can be engineered to achieve maximum absorption efficiency and, therefore, optimal imaging response. This was shown in the image quality differences at 2.8 and 3.6 THz when imaging using the IR-160 silicon nitride-based microbolometer. As we have seen in this thesis, improved microbolometer performance in the IR spectral range does not necessarily translate into enhanced performance in the THz spectral range, and that there are technical limits to the success of modified IR microbolometers as THz imaging detectors.

Finally of interest to the author was the notion that current camouflage technologies for concealing military assets might easily be exploited by a THz imaging system. Of the numerous materials analyzed only one showed promise, the camouflage net and it happens to be the mainstay for concealing mobile military assets by countries around the world. The clear images of the knife concealed by the THz transparent single camouflage leaf can easily be extrapolated to an artillery piece concealed by an entire camouflage net. The outstanding results from this proof-of-principle experiment indicate that THz imaging holds promise for battlefield sensing so long as improvements to sources and detectors continue to be made.

There are several avenues for further research suggested by our work. In particular, it is evident from the images of the concealed knife blade that the experimental setup could be improved. In particular, the images exhibit pronounced background interference fringes and/or diffraction patterns, which seriously degrade the target field-to-background signal-to-noise properties of the images. If their interference effects can be understood and then suppressed during later experiments, significantly greater target discrimination should result. Several interferences may be drawn from the images. First,

notice in Figure 39, 41 and 42 narrow regions of the target knife blade do not appear to produce edge diffraction fringes. This suggests that the high-contrast fringes surrounding the blade image are artifacts of the optical setup, rather than the target object. Second, the fringes appear to have an eccentric geometry, rather than one that is circularly symmetrical about the beam axis. This, as well as the total absence of linear Haidinger fringes, indicates that optically flat components such as windows, are not the culprits. Third, the fringe eccentricity strongly resembles the phase-space footprint that would be produced by an off-axis conic section. Two such components exist in our setup, namely the paraboloidal mirrors. These mirrors are standard components, manufactured for use at much shorter wavelengths than those used here. At wavelengths on the order of 1 mm, the optical coatings on these mirrors are extremely thin, much thinner than the radiation's skin depth. We speculate then, that the background interference fringes arise from the off-axis paraboloidal mirrors. By using alternative components machined from solid metallic blocks, such as bulk aluminum, it may be possible to suppress the fringes. This could be tested quite easily because, at millimeter wavelengths, high quality optical surfaces can be fabricated using standard machining methods. Expensive optically figured surfaces are not needed at all. Indeed, such machined components could replace the 90° off-axis configuration shown in Figure 23, which is far from ideal, because the paraboloids' focal surfaces are severely inclined to the optical axis. The testing of these hypotheses could form the basis for follow-on research to this thesis project.

THIS PAGE INTENTIONALLY LEFT BLANK

LIST OF REFERENCES

- [1] M.C. Kemp, P.F. Taday, B.E. Cole, J.A. Cluff, A.J. Fitzgerald, and W.R. Tribe, "Security applications of terahertz technology," *Proc. SPIE* **5070**, 44-52 (2003).
- [2] M.B. Campbell, and E.J. Heilweil, "Non-invasive detection of weapons of mass destruction using THz radiation," *Proc. SPIE* **5070**, 38-43 (2003).
- [3] R. Osiander, J.A. Miragliotta, Z. Jiang, J. Xu, and X.C. Zhang " Mine Field Detection and Identification Using THz Spectroscopic Imaging," *Proc. SPIE* **5070**, 1-6 (2003).
- [4] M.J. Fitch, D. Schauki, C.A. Kelly, R. Osiander, "THz Imaging and Spectroscopy for Landmine Detection," *Proc. SPIE* **5354**, 45-54 (2004).
- [5] J.F. Federici, D. Gary, R. Barat, and D. Zimdars, "THz Standoff Detection and imaging of Explosives and Weapons," *Proc. SPIE* **5781**, 75 (2005).
- [6] E.L. Jacobs, and S. Moyera, "Concealed weapon identification using terahertz imaging sensors," *Proc. SPIE* 6212, 1-10 (2006).
- [7] J.E. Bjarnason, T.L.J. Chan, A.W.M. Lee, M.A. Celis and E.R. Brown, "Millimeter-Wave terahertz, and mid-infrared transmission through common clothing," *Appl. Phys. Lett.* **85**, 519-521 (2004).
- [8] A.J. Gatesman, A. Danylove, T.M. Goyette, J.C. Dickinson, R.H. Giles, W. Goodhue, J. Waldman, W.E. Nixon, and W. Hoen, "Terahertz behavior of optical components and common materials," *Proc. SPIE* **6212**, 62120E (2006).
- [9] M.C. Kemp, A. Glauser, C. Baker, "Recent developments in people screening using terahertz technology – seeing the world through terahertz eyes," *Proc SPIE* **6212**, 62120T1-10 (2006).
- [10] Agilent Laboratories (January 2004). *Imaging at 3.4 THz with a Quantum Cascade Laser* from Power Point presentation.
- [11] D.R. Chamberlain, P.R. Robrish, W.R. Trutna, G. Scalari, M. Giovannini, L. Ajili and J. Faist, "Imaging at 3.4 THz with a quantum-cascade laser," *Appl. Opt.* **44**, 121-125 (2005).
- [12] A.W.M. Lee and Q Hu, "Real-Time, continuous-wave terahertz imaging by use of a microbolometer focal-plane array," *Opt. Lett.* **30**, 2563-2565 (2005).

- [13] A.W.M. Lee, B.S. Williams, S. Kumar, Q. Hu, and J.L Reno, "Real Time Imaging Using a 4.3-THz Quantum Cascade Laser and a 320X240 Microbolometer Focal Plane Array," *IEEE Photon. Tech. Lett.* **18**, 1415 (2006).
- [14] A.W.M. Lee, Q. Qui, S. Kumar, B.S. Williams, and Q. Hu, "Real-time terahertz imaging over a standoff distance (>25 meters)," *App. Phys. Lett.* **89**, 141125 (2006).
- [15] M. Lowe, *Imaging of 3.4 THz Quantum Cascade Laser Beam using Uncooled Microbolometer Camera*, M.S. Thesis, Naval Postgraduate School, Dec. 2006.
- [16] B.N. Behnken, *Real-Time Terahertz Imaging using a Quantum Cascade Laser and Uncooled Microbolometer Focal Plane Array*, Ph. D. Dissertation, Naval Postgraduate School, Mar. 2008.
- [17] B.N. Behnken, G. Karunasiri, D.R. Chamberlin, P.R. Robrish, and J. Faist, "Real-time imaging using a 2.8 THz quantum cascade laser and uncooled infrared microbolometer camera," *Opt. Lett.* **33**, 440-442 (2008).
- [18] B.N. Behnken, G. Karunasiri, D.R. Chamberlin, P.R. Robrish, and J. Faist, "Optimization of a 3.6-THz Quantum Cascade Laser for Real-Time Imaging with a Microbolometer Focal Plane Array," *Proc. SPIE* **6893**, 6893-22 (2008).
- [19] M. Tonouchi, "Cutting Edge terahertz technology," *Nature Photonics* **1**, 97-105 (2007).
- [20] S.R. Murrill, E.L. Jacobs, S.K. Moyer, C.E. Halford, S.T. Griffin, F.C. De Lucia, D.T. Petkie, and C.C. Franck, "Terahertz imaging system performance model for concealed-weapon identification," *App. Opt.* **47**, 1286-1297 (2008).
- [21] M.A. Belkin, F. Capasso, F. Xie, A. Belyanin, M. Fischer, A. Wittmann, and J. Faist, "Room temperature terahertz quantum cascade laser source based on intracavity difference-frequency generation," *Appl. Phys. Lett.* **92**, 201101 (2008).
- [22] A. Tredicucci, L. Mahler, T. Losco, J. Xu, C. Mauro, R. Kohler, H.E. Beere, D.A. Ritchie, E.H. Linfield, "Advances in THz quantum cascade lasers: fulfilling the application potential," *Proc. SPIE* **5738**, 146-153 (2005).
- [23] Infrared Solutions, Inc. IR-160 Thermal Imager product information sheet (2004).
- [24] Thermoteknix Systems Ltd. Miricle 110K Model specifications (2007).

- [25] R. F. Kazarinov and R. A. Suris, "Possibility of amplification of electromagnetic waves in a semiconductor with a superlattice," *Fizika I Tekhnika Poluprovodnikov* **5**, 797-800 (1971).
- [26] J. Faist, F. Capasso, D. L. Sivco, C. Sirtori, A. L. Hutchinson, and A. Y. Cho, "Quantum cascade laser," *Science* **264**, 553-556 (1994).
- [27] B.S. Williams, "Terahertz quantum cascade lasers," *Nature photonics* **1**, 517-525 (2007).
- [28] L. Ajili, G. Scalari, D. Hofstetter, M. Beck, J. Faist, H. Beere, G. Davies, E. Linfield, and D. Ritchie, "Continuous-wave operation of far-infrared quantum cascade lasers," *Electron. Lett.* **38**, 1675-1676 (2002).
- [29] M. Rochat, L. Ajili, H. Willenberg, J. Faist, H. Beere, G. Davies, E. Linfield and D. Ritchie, "Low-threshold terahertz quantum-cascade lasers," *Appl. Phys. Lett.* **81**, 1381-1383 (2002).
- [30] G. Scalari, L. Ajili, J. Faist, H. Beere, D. Ritchie, E. Linfield, G. Davies, "Far-infrared ($\lambda=87\mu\text{m}$) bound-to-continuum quantum cascade lasers operating up to 90K," *Appl. Phys. Lett.* **82**, 3165-3167 (2003).
- [31] L. Ajili, G. Scalari, J. Faist, H. Beere, G. Davies, E. Linfield, and D. Ritchie, "High power quantum cascade lasers operating at $\lambda=87$ and $130\mu\text{m}$," *Appl. Phys. Lett.* **84**, 3986-3988 (2004).
- [32] Rosencher and Vinter, *Optoelectronics*, Cambridge, U.K., University Press, 2002.
- [33] R. G. Buser and M. F. Tompsett, "Historical Overview," in *Semiconductors and Semimetals 47: Uncooled Infrared Imaging Arrays and Systems*, P. W. Kurse and D.D. Skatrud, ed. (Academic Press, San Diego, 1997).
- [34] P. W. Kurse, "Principals of uncooled infrared focal plane arrays," in *Semiconductors and Semimetals 47: Uncooled Infrared Imaging Arrays and Systems*, P. W. Kurse and D.D. Skatrud, ed. (Academic Press, San Diego, 1997)
- [35] E.L. Dereniak and G.D. Boreman, *Infrared Detectors and Systems*, John Wiley and Sons, New York, NY, 1996.
- [36] G. Karunasiri, X. Gu, G. Chen and U. Sridhar, "Extraction of Thermal Parameters of Microbolometer Infrared Detectors Using Electrical Measurements," *Proc. SPIE* **3436**, 668-674 (1998).
- [37] S.R. Ravi, G. Karunasiri, "Electro-thermal modelling of infrared microemitters using PSPICE," *Sensors and Actuators* **A72**, 110-114 (1999).

- [38] R. A. Wood, "Monolithic silicon microbolometer arrays," in *Semiconductors and Semimetals 47: Uncooled Infrared Imaging Arrays and Systems*, P. W. Kurse and D.D. Skatrud, ed. (Academic Press, San Diego, 1997).
- [39] M.J. Rosker, and H.B. Wallace, "Imaging Through the Atmosphere at Terahertz Frequencies," *IEEE 1-4244-0688-09*, 773-776 (2007).
- [40] F.G. Smith, ed. "Atmospheric propagation of radiation," Vol. 2 in *The Infrared and electro-optical systems handbook*, J.S. Accetta and D.L. Shumaker, ed. (Infrared Information Analysis Center, Ann Arbor, Michigan and SPIE Optical Engineering Press, Bellingham, Washington 1997).
- [41] RIKEN THz database www.riken.jp/THzdatabase (Tera-photonics Laboratory, RIKEN Sendai, 4 Nov 2008)
- [42] D.H. Pollock, ed. "Countermeasure systems," Vol. 7 in *The Infrared and electro-optical systems handbook*, J.S. Accetta and D.L. Shumaker, ed. (Infrared Information Analysis Center, Ann Arbor, Michigan and SPIE Optical Engineering Press, Bellingham, Washington 1997).

INITIAL DISTRIBUTION LIST

1. Defense Technical Information Center
Ft. Belvoir, Virginia
2. Dudley Knox Library
Naval Postgraduate School
Monterey, California
3. Director General Land Equipment Program Management
Ottawa, Ontario
4. Professor Gamani Karunasiri
Naval Postgraduate School
Monterey, California
5. Professor Scott Davis
Naval Postgraduate School
Monterey, California
6. Professor James Luscombe
Naval Postgraduate School
Monterey, California